**Title: Identification of a Binding Site for Small Molecule Inhibitors Targeting Human TRPM4**

**Authors**

Babatunde Ekundayo[1], Prakash Arullampalam[2], Christian E. Gerber[2], Anne-Flore Hämmerli[2], Sabrina Guichard[2], Mey Boukenna[2], Daniela Ross[2], Martin Lochner[2], Jean-Sebastien Rougier[2], Henning Stahlberg[1]*, Hugues Abriel[2]*, and Dongchun Ni[1]

**Affiliations**

[1] Laboratory of Biological Electron Microscopy, IPHYS, SB, EPFL, and Dept. Fundamental Microbiology, Faculty of Biology and Medicine, UNIL, Cubotron, Rt. de la Sorge, 1015 Lausanne, Switzerland.

[2] Institute of Biochemistry and Molecular Medicine and Swiss National Centre of Competence in Research TransCure, University of Bern, Bern, Switzerland

* Corresponding authors: henning.stahlberg@epfl.ch, hugues.abriel@unibe.ch

## Abstract:

Transient receptor potential (TRP) melastatin 4 (TRPM4) protein is a calcium-activated monovalent cation channel associated with various genetic and cardiovascular disorders. The anthranilic acid derivative NBA is a potent and specific TRPM4 inhibitor, but its binding site in TRPM4 has been unknown, although his information is crucial for drug development targeting TRPM4. We determined the cryo-EM structures of full-length human TRPM4 embedded in native lipid nanodiscs in an unbound, a state bound to NBA, and a new anthranilic acid derivative known as IBA-bound state. We found that the small molecules NBA and IBA were bound in a pocket formed between the S3, S4, and TRP helices and the S4-S5 linker of TRPM4. Our structural data and results from patch clamp experiments enable validation of a binding site for small molecule inhibitors, paving the way for further drug development targeting TRPM4.

# Main text

## Introduction

Transient receptor potential (TRP) ion channels are a superfamily of cation channels involved in various physiological functions, including sensory perception, cellular homeostasis, and ion transport [1,2]. Mutations in the genes encoding TRP ion channels that lead to their dysfunction or dysregulation, have been implicated in numerous diseases and genetic disorders. Therefore, TRP channels are attractive therapeutic targets for drug development [3,4].

The TRPM (melastatin-like transient receptor potential) sub-family member, TRPM4, is a calcium-activated non-selective monovalent cation channel. The voltage-dependent activation of TRPM4 by intracellular calcium drives a current due to monovalent cations flux such as $Na^+$ and $K^+$ through the channel, leading to plasma membrane depolarization facilitating, in many cell types, calcium uptake via other calcium-permeable channels [5,6]. TRPM4 activity regulates physiological processes such as cardiac conduction, smooth muscle contraction, insulin secretion, and immune responses [7–9]. Genetic defects in *TRPM4* have been found in patients with inherited cardiac conduction disorders. Furthermore, alterations of TRPM4 function have been linked to diabetes, hypertension, and cancer [10–16]. Thus far, several small molecules identified and developed as potent and selective TRPM4 inhibitors are used as research tools to investigate the potential of TRPM4 as a therapeutic target and are promising candidates for drug development [17]. These molecules include 9-phenanthrol, flufenamic acid and the anthranilic acid derivatives CBA (4-chloro-2-[2-(2-chloro-phenoxy)-acetylamino]-benzoic acid) and NBA (4-chloro-2-(2-(naphthalene-1-yloxy) acetamido) benzoic acid [18–21]. NBA and CBA are thus far the most selective and potent TRPM4 inhibitors reported; however, it remains unknown how these drugs bind and inhibit TRPM4 activity [19]. To facilitate drug development targeting TRPM4, detailed structural information revealing the mode of binding these molecules to TRPM4 is essential.

Cryo-electron microscopy (cryo-EM) enabled the structure determination of several TRP channels and revealed the druggable sites in these channels by structure determination in the presence of antagonists and drug molecules [3,17]. These structures have revealed different drug-binding pockets around the TRP channels' transmembrane domains (TMD). For example, the synthetic molecule icilin binds into a hydrophobic pocket of the Voltage Sensor Like Domain (VSLD) in TRPM8 and the binding of the small molecule inhibitor NDNA (*N′*-(3,4-dimethoxybenzylidene)-2-(naphthalen-1-yl)acetohydrazide) into the cavity between the S1-S4 domain and pore domain of TRPM5 [22,23]. These two examples revealed different drug-binding sites within the same subfamily of TRP channels. Interestingly, lipid molecules can share binding sites with drug molecules and inhibit drug binding and activity, as demonstrated in the binding of 2-ABP (2-aminoethyl diphenylborinate) into the VBP (Vallanoid Binding Pocket) of TRPV2, which could be inhibited by binding an endogenous cholesterol molecule [24].

Structures of detergent-isolated TRPM4 studied by cryo-EM have revealed the binding sites of the cholesterol homolog CHS (Cholesteryl Hemisuccinate) used to purify TRPM4, suggesting potential endogenous cholesterol binding sites [25–28]. However, to date there are no reported structures of TRPM4 bound to specific inhibitors. It is also possible that the addition of CHS required for stabilizing TRPM4 during detergent isolation could occlude potential drug-binding sites. To address this problem, we have isolated TRPM4 in its native lipid environment using SMA (Styrene Maleic Anhydride) nanodiscs and determined its high-resolution structure in the presence and absence of the small molecules NBA and a new derivative IBA (4-chloro-2-[2-(3-iodophenoxy)-acetylamino]-benzoic acid) which has a similar potency to NBA (**Figure 1; Figure 2a-c and Supplementary Fig. 1- 8**) [29]. These structures reveal the mode of binding and inhibition of two potent and specific TRPM4 inhibitors, paving the way for future drug development and facilitating further investigations of TRPM4 as a therapeutic target for treating related maladies.

## Results

### Structures of HsTRPM4 in its native lipid environment

We determined cryo-EM structures of full-length human TRPM4 in endogenous lipid nanodiscs in apo ($HsTRPM4_{apo}$), IBA ($HsTRPM4_{IBA}$) and NBA ($HsTRPM4_{NBA}$) bound states at overall resolutions of 3.7, 3.6 and 4.5 Å respectively (**Figure 1; Figure 2; Supplementary Fig. 4- 8; Supplementary Table 1**). All structures obtained were identical to previously determined cryo-EM structures of TRPM4 in detergent micelles and reconstituted nanodiscs [25–28]. However, we found that in native nanodiscs, densities for the cytosolic regions of TRPM4 were poorly resolved than previously determined structures resulting in lower-resolution 3D reconstructions in these regions, which could be a result of TRPM4 solubilization using SMA. This effect was more pronounced in the cytosolic N-terminal TRPM homology regions 1 and 2 (MHR1/ 2), with the density in these regions being much less defined (**Supplementary Fig. 1c; Supplementary Fig. 2a and b**). Therefore, 3D reconstructions could not be obtained for these regions (**Supplementary Fig. 2; 4- 6**). These results suggest that SMA solubilization results in a less stable TRPM4 structure, which could result from the differences in lipid composition or binding compared with structures of TRPM4 in detergent micelles and reconstituted nanodiscs. Indeed, examination of the TMD revealed that although the structural arrangement of the transmembrane helices was identical, the lipid arrangement was strikingly different from previously determined TRPM4 structures [25–28]. Notably, the published structure of HsTRPM4 in a reconstituted lipid nanodisc as well as cryo-EM density maps of detergent-solubilized HsTRPM4 and MmTrpm4 from this study, revealed ordered densities for annular phospholipids and three CHS molecules, one of which (CHS-2) occludes the drug binding site (**Supplementary Fig. 2 and 3; Supplmentray Table 2)** [26].

On the other hand, in our structures, ordered densities for annular lipids are markedly reduced, with primarily three densities for cholesterol molecules bound to TRPM4 observed (**Figure 1a -d; Supplementary Fig. 2a and b**). Of the three, two cholesterol molecules

(CHR-1 and CHR-2) bind in similar positions to CHS molecules in a previous structure in a reconstituted nanodisc (**Supplementary Fig. 2a and b**). One of these molecules (CHR-1) interacts with the S6 helix close to the channel pore, and another (CHR-2) in a pocket formed between S3 and S4 helices and the S4-S5 linker equivalent to the VBP of TRPV2; however, the density for this cholesterol molecule is weak, suggesting low occupancy (**Figure 1e -f**). The third cholesterol molecule (CHR-3) in our structures binds between the S5 and S2 helix from an adjacent protomer differing from the previously reported position of CHS at the pre-S1 elbow (**Supplementary Fig. 2a -c**). The presence of less density for annular lipids in the native nanodiscs was an important factor that enables assignment of density for the drugs in the HsTRPM4$_{IBA}$ and HsTRPM4$_{NBA}$ structures (**Supplementary Fig. 8**).

**The binding site of the small molecule inhibitors NBA and IBA in HsTRPM4**

Analysis of the HsTRPM4$_{IBA}$ and HsTRPM4$_{NBA}$ structures revealed discrete densities for the IBA and NBA molecules located at the periphery of the inner membrane leaflet in the pocket formed between S3 and S4 helices, S4-S5 linker and TRP helix (**Figure 2d- i**). The presence of the ligands in this pocket suggests that these ligands can displace the endogenous cholesterol molecule (CHR-3) present in the HsTRPM4apo structure, which is possibly not tightly bound as judged by the weaker density map for this molecule compared to other bound cholesterol molecules (**Figure 1e and f)**. Ligand binding induces only very subtle conformational changes in the structure of HsTRPM4, with the overall structures remaining broadly similar (**Figure 2j -l**). The HsTRPM4 ion conduction pore is also in the closed state in all three structures. Although changes in the pore radius profile are observed in the IBA-bound structure, these are due to side chain rotamer differences of a few residues lining the pore. These changes are negligible as the pore remains in a closed state (**Figure 2l**). Interestingly, apparent density for $Ca^{2+}$ could be observed in cryo-EM density maps of our structures of TRPM4 in native nanodiscs, which suggests the possible binding of endogenous $Ca^{2+}$ ions however this did not result in an open state of the channel

(**Supplementary Fig. 9**). Both IBA and NBA share a common anthranilic acid moiety but differ in that NBA possesses an additional ring of its naphthalene substituent, making it bulkier and more hydrophobic than the smaller 3-iodophenyl ring of IBA (**Figure 2e and h, Supplementary Fig. 8**). In both $HsTRPM4_{IBA}$ and $HsTRPM4_{NBA}$ structures, the hydrophilic anthranilic acid moiety containing acidic, amide and chloride groups faces towards the cytosol and interacts with charged amino acid side chains from TRPM4 (**Figure 3a and b; Supplementary Fig. 7d and e**). Notably, the anthranilic acid moiety interacts with His908 from the S4 helix, Tyr1057, Gln1061, and Arg1064 from the TRP helix as well as with Ser924 from the S4-S5 linker, and Ser863 from the S3 helix in both structures (**Figure 3a and b**). These interactions between the anthranilic acid moiety and residues of TRPM4 reveal the chemical basis behind the specific binding of the anthranilic acid derivatives to TRPM4.

NBA and IBA have a similar potency for TRPM4 inhibition, possibly by making additional unknown interactions in the binding pocket [19–20]. Our structures show that the naphthalene substituent and the 3-iodophenyl ring of NBA and IBA bind into a hydrophobic pocket between the S3 and S4 helices of TRPM4 (**Figure 4a and b; Supplementary Fig. 7d and e**), making hydrophobic interactions with the residues that decorate this pocket, including Val901, Val904 and Leu907 (**Figure 3b and c**). Therefore, these structures reveal a rationale for the potency and specificity of NBA and IBA and pave the way for designing chemical modifications of these molecules to enable increased targeting of the binding pocket to develop more potent and specific inhibitors.

**Validation of the NBA and IBA binding site in HsTRPM4**

To disrupt the drug-protein interactions in the hydrophilic region of the drug binding site, we introduced the HsTRPM4 mutations Ser863Ala, His908Ala, Ser924Ala, Lys925Ala, Tyr1057Ala, Gln1061Ala, Arg1064Ala, Arg1064Gly, Arg1064Ser, and the double variant Ser863Ala/ Ser924Ala. Additional Val901Trp and Val904Trp are space-filling mutations that

disrupt the hydrophobic pocket—introducing these mutations aimed to reduce the drug's inhibitory effect compared to wildtype HsTRPM4. As proof of concept, the experiments were done with NBA only since it shares a binding site similar to that of IBA. First, the expression of the different variants was investigated using the western blot approach (**Supplementary Fig. 10 a and b**). Only Ser863Ala and Gln1061Ala variants showed a significantly reduced expression compared to the wildtype channel (**Supplementary Fig. 10 a and b**). In parallel, functional experiments revealed that after activation of the HsTRPM4 function by adding 300 µM of free calcium, almost all variants decreased in function except Ser863Ala, Ser924Ala, Arg1064Ala, and Arg1064Gly (**Supplementary Fig. 10c, 11 and 12**). Due to the reduction of activation in these mutants, we wondered if this decrease in function observed may be due to an alteration of the calcium sensitivity of those variants. The calcium sensitivity curves performed on some loss-of-function HsTRPM4 variants (Val904Trp, Tyr1057Ala, Gln1061Ala, Arg1064Ser, and the double variant Ser863Ala/ Ser924Ala) show that the different $EC_{50}$s for calcium are not higher (less sensitivity to calcium-free) compared to wildtype HsTRPM4 suggesting that this decrease of function may not entirely be to a reduction of calcium sensitivity (**Supplementary Fig. 13a**). On the contrary, the different $EC_{50}$s of the variants are smaller than the wildtype $EC_{50,}$ suggesting an increase in this calcium sensitivity (**Supplementary Fig. 13a**). Following those experiments and knowing that the inhibitory effect mediated by NBA will be investigated on these variants in the presence of calcium (to activate them), control experiments were performed using HsTRPM4 wildtype channels to explore the potential influence of NBA on calcium sensitivity. The results showed no drastic difference in the $EC_{50}$s was observed, suggesting that NBA does not alter the calcium sensitivity of the wildtype channels (**Supplementary Fig. 13b**). The absence of the effect of NBA and amino acid mutations on calcium sensitivities leads us to perform the final experiment investigating the consequences of modifying those amino acids on the inhibitory effect mediated by NBA. As a proof of concept, the mutations Ser863Ala, Val901Trp, His908Ala, Ser924Ala, Arg1064Ala, Arg1064Gly, and the double variant Ser863Ala/ Ser924Ala were investigated. Compared to wildtype HsTRPM4, NBA dose-effect

curves on single variants of the HsTRPM4 channel show a drastic reduction (one log of difference) of the $IC_{50}$s for the NBA (**Figure 3e**). Compared to the wildtype construct, a more pronounced decrease in the efficiency of NBA (two logs of difference) is observed in the presence of double mutation (**Fig. 3e; Figure 4; Supplementary Figure 14**). In addition, a control experiment has been performed using a mutant of HsTRPM4 linked to cardiac dysfunction and already reported in the literature; the mutant HsTRPM4 T677I [30]. This variant has been selected based on the presence outside the putative NBA binding of the mutated amino acid and because this point mutation did not alter the biophysical properties of the channel [30]**.** This mutation did not alter the $IC_{50}$ of the NBA, as observed with the NBA binding pocket variants (**Figure 3f and g**). Overall, these data strongly support the notion that those amino acids of HsTRPM4 are part of the binding pocket for NBA/ IBA determined from our cryo-EM structures.

## Discussion

We have utilized cryo-EM to determine the high-resolution structures of HsTRPM4 bound to specific inhibitors. Importantly, we find that using SMA to isolate HsTRPM4 in its endogenous lipid nanodisc was necessary to unequivocally assign densities for the inhibitor molecules. This finding supports the relevance of previous attempts to isolate TRPM4 in its native lipid environment but unfortunately yielded lower resolution structures [31]. High-resolution structures of TRPM4 have previously been determined in detergent micelles and in reconstituted lipid nanodiscs, both of which require detergent isolation of the protein from the cell and, by so doing, introduce artefacts to the lipid environment of the protein. An essential factor is that the added CHS, to maintain protein stability in detergent extraction, binds in specific sites in the protein, which may or may not represent actual cholesterol binding. We observed apparent differences in the binding arrangement of annular lipids to TRPM4 from the structural data when isolated with SMA. Most striking is that a CHS molecule completely occupies the drug binding site, suggesting that obtaining a structure or performing biochemical experiments with detergent-CHS isolated protein and these

inhibitors does not represent the endogenous scenario. Indeed, in our previous attempts to determine the structure of detergent-isolated TRPM4 in complex with NBA/ IBA, the identification of the inhibitor binding site was ambiguous. This finding also shows the importance of the composition and binding arrangement of the lipid annulus to the function and inhibition of the target membrane protein. This study shows that using SMA would be advantageous for the structure determination of drugs with membrane proteins, particularly in cases where the drug binds in the TMD exposed to lipid molecules.

Although there are no structures of TRPM4 in its open state available, movement of the TRP helix is required for the activation of the TRPM2 channel and the relative movement of the TRP helix to S1-S4 helices is shown to be required for desensitization of the TRPM8 channel[32,33]. These findings hint towards a role of TRP helix movement in regulating the channel pore of the TRPM subfamily. The binding of NBA/ IBA to TRPM4 may restrict the movement of the TRP helix, maintaining the TRPM4 channel pore in a closed state even in the presence of activation stimuli, but structures of HsTRPM4 in the open state would be necessary to determine whether this is the case or not. The role of the bound cholesterol molecule in the same pocket remains unclear. This cholesterol could also regulate channel function in response to changes in the membrane environment.

Our study has identified the binding pocket for inhibiting TRPM4 for the anthranilic acid derivatives (**Figure 5**). These drugs bind in a pocket between S3 and S4 helices, S4-S5 linker and TRP helix. However, detailed insights into the mechanism of inhibition will require structure determination of TRPM4 in its open state, which so far has been elusive. It is clear that the addition of $Ca^{2+}$ ions is not sufficient to obtain the open sate with purified TRPM4 in lipid nanodiscs, and the presence of a membrane potential may be necessary. Our future studies will seek to address this. Nonetheless, the identification of a binding pocket for TRPM4 inhibitors presents a significant milestone towards further development of new potent and even more specific drugs targeting the TRPM4 ion channel for therapeutic intervention.

**Acknowledgements**

This work was supported by the Swiss National Science Foundation (SNF Grants CRSII5_177195 and the NCCR TransCure (185544)). We thank Emiko Uchikawa, Sergey Nazarov, Bertrand Beckert and members of the DCI-Lausanne from EPFL, UNIL, and UNIGE for their support. We thank Kelvin Lau, Florence Pojer, Laurence Durrer and Soraya Quinch the PTPSP at EPFL for their support with protein expression.

**Author Contributions Statement**

HS and HA conceptualized the project. BE and DN performed cryoEM sample preparation and structure determination with support from the DCI-Lausanne. PA, AH, SG, DR and MB performed biochemistry and patch clamp experiments. CEG. and ML designed the target molecule IBA and synthesis. CEG. performed the synthesis of NBA and IBA. HS and HA acquired funding. Project administration and supervision was done by BE and JR. Writing original draft was done by BE. Manuscript review & editing was done by DN, BE, JR, ML, HA and HS. All authors read and approved the manuscript.

**Competing Interests Statement**

The authors declare no competing interests.

**Supplementary Table 1**

| Data collection and processing | HsTRPM4apo (EMD-19057) (PDB 8RCR) | HsTRPM4IBA (EMD-19061) (8RCU) | HsTRPM4NBA (EMD-19069) (PDB 8RD9) (EMD-19060, local) |
|---|---|---|---|
| Nominal Magnification | 165kx | 165kx | 165kx |
| Voltage (kV) | 300 | 300 | 300 |
| Recorded Micrographs | 6 429 | 7 500 | 11 851 |
| Electron exposure ($e^-/Å^2$) | 50 | 50 | 50 |
| Defocus range (μm) | 0.8-2.5 | 0.8-2.5 | 0.8-2.5 |
| Pixel size (Å) | 0.726 | 0.726 | 0.726 |
| Symmetry imposed | C4 | C1/C4 | C4 |
| Initial particle images (no.) | 1 719 323 | 1 149 090 | 1 805 182 |
| Final particle images (no.) | 16 308 | 20 345 | 15 954 |
| Map resolution (Å) | 3.67 | 3.59 | 4.50 |
| FSC threshold | 0.143 | 0.143 | 0.143 |
| Map resolution range (Å) | 30-3.3 | 30-3.2 | 30-3.6 |
| Map sharpening B factor ($Å^2$) | -69.7 | -52.2 | -108.1 |
| | | | |
| **Refinement** | | | |
| Initial model used (PDB code) | 6BQV | 6BQV | 6BQV |
| Model composition<br>Non-hydrogen atoms<br>Protein residues<br>Ligands | <br>8<br>2420<br>CHR: 12 | <br>9<br>2420<br>IBA: 4<br>CHR: 8 | <br>8<br>2422<br>NBA: 4<br>CHR: 8 |
| *B* factors ($Å^2$)<br>Protein<br>Ligand | <br>41.23/251.46/135.21<br>63.19/103.12/79.00 | <br>0.00/93.44/38.86<br>15.44/136.15/47.75 | <br>142.10/427.50/239.20<br>20.00/33.04/22.07 |
| R.m.s. deviations<br>Bond lengths (Å)<br>Bond angles (°) | <br>0.012 (146)<br>0.801 (7) | <br>0.003 (0)<br>0.721 (0) | <br>0.004 (0)<br>0.925 (10) |
| Validation<br>MolProbity score<br>Clashscore<br>Poor rotamers (%) | <br>1.93<br>14.67<br>0.00 | <br>2.04<br>16.76<br>0.19 | <br>2.23<br>24.33<br>0.05 |
| Ramachandran plot<br>Favored (%)<br>Allowed (%)<br>Disallowed (%) | <br>96.16<br>3.71<br>0.13 | <br>95.49<br>4.34<br>0.17 | <br>94.82<br>4.76<br>0.42 |

**Supplementary Table 1 | Cryo-EM data collection, refinement and validation statistics for SMA solubilized HsTRPM4 samples.**

**Supplementary Table 2**

| Data collection and processing | HsTRPM4+Ca2<br>EMD-19072 | HsTRPM4+NBA+$Ca^{2+}$<br>EMD-19073 | MmTRPM4+$Ca^{2+}$<br>EMD-19074 |
|---|---|---|---|
| Nominal Magnification | 96kx | 96kx | 165kx |
| Voltage (kV) | 300 | 300 | 300 |
| Recorded Micrographs | 11 877 | 10 219 | 8 313 |
| Electron exposure ($e^-$/Å$^2$) | 40 | 40 | 60 |
| Defocus range (μm) | 0.8-2.5 | 0.8-2.5 | 0.8-2.5 |
| Pixel size (Å) | 0.83 | 0.83 | 0.726 |
| Symmetry imposed | C4 | C4 | C4 |
| Initial particle images (no.) | 4 430 540 | 2 774 028 | 4 340 237 |
| Final particle images (no.) | 128 316 | 40 061 | 100 227 |
| Map resolution (Å) | 3.04 | 2.98 | 2.87 |
| FSC threshold | 0.143 | 0.143 | 0.143 |
| Map resolution range (Å) | 30-2.6 | 30-2.5 | 30-2.5 |

**Supplementary Table 2 | Cryo-EM data collection for DDM/CHS solubilized HsTRPM4 and MmTRPM4 samples.**

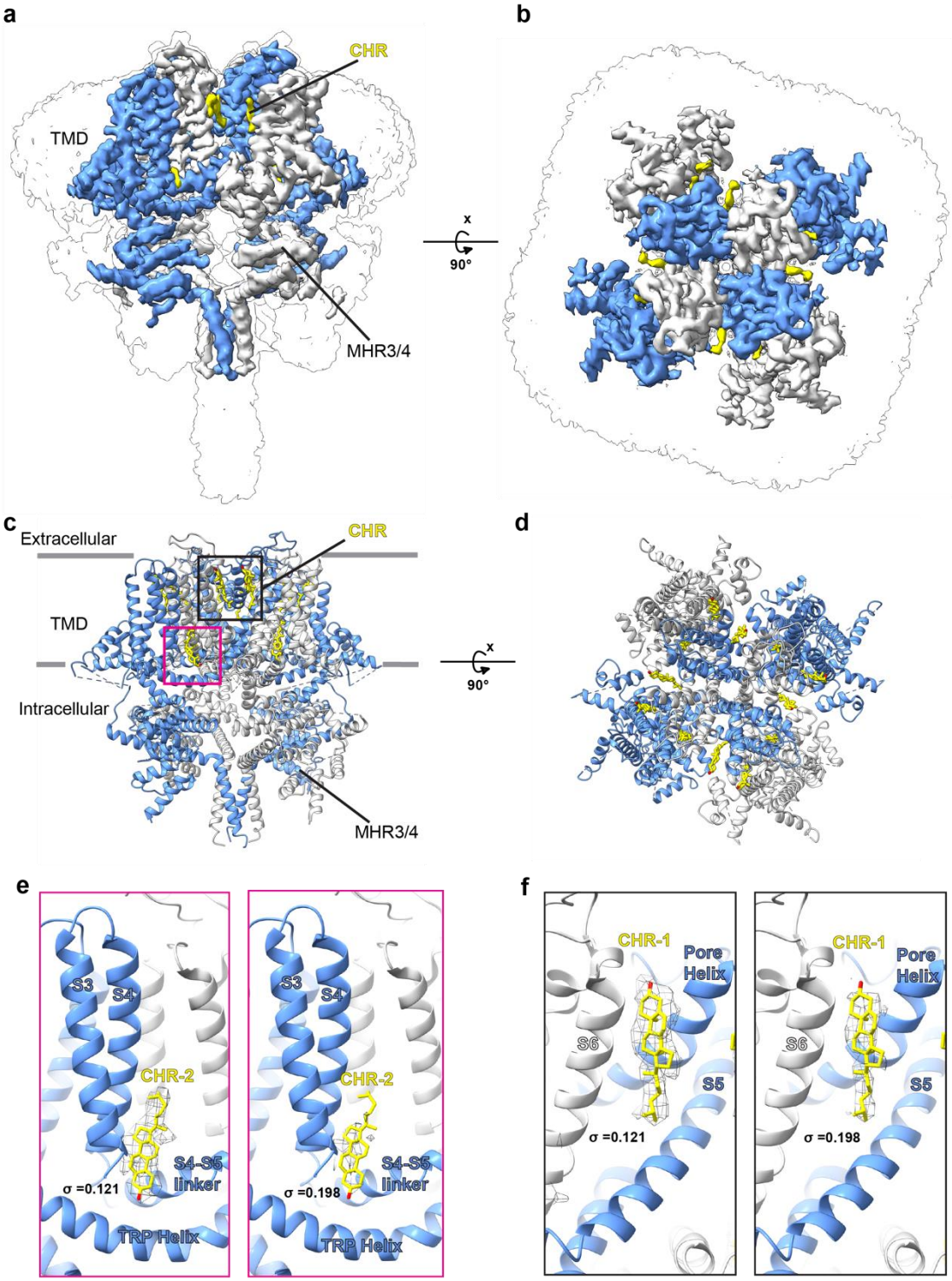


**Figure 1**: Overall structure of HsTRPM4$_{apo}$ in native lipid nanodiscs. (a and b) Cryo-EM densities in surface representation of HsTRPM4$_{apo}$ in two views. Alternating protomers of TRPM4 are shown in blue and white. (c and d) Cartoon representation of the HsTRPM4$_{apo}$ corresponding to the cryo-EM densities in a and b. The positions of

bound cholesterol molecules (CHR) are indicated. The black box indicates the position of CHR-1 and CHR-3 shown in yellow. In contrast, the pink box indicates the position of CHR-2. (e) Cryo-EM density in mesh representation for CHR-2 (f) Cryo-EM density in mesh representation for CHR-1. In e and f, the density threshold level is indicated by σ.

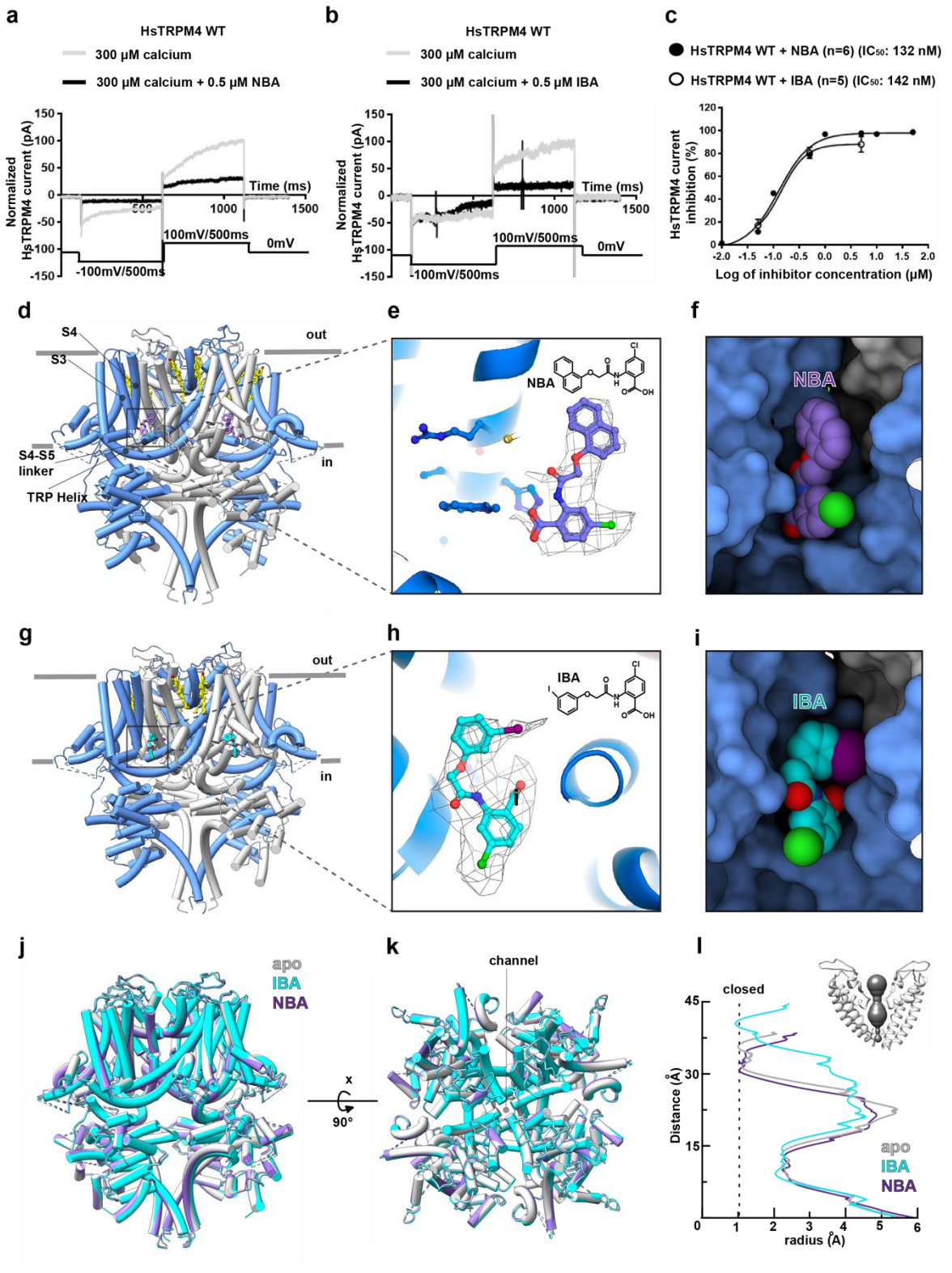


**Figure 2**: Structures of HsTRPM4$_{NBA}$ and HsTRPM4$_{IBA}$. (a) Representative sodium calcium-activated HsTRPM4 current traces of wildtype (WT) HsTRPM4 in the presence of 300 µM of calcium (grey line) and in the presence of both calcium and

0.5 µM of NBA (black line). (b) In the presence of 300 µM of calcium (grey line) and both calcium (grey line) and 0.5 µM of IBA (black line). (c) NBA and IBA dose-response curves of wildtype (WT). (n): number of cells. (d) The structure of $HsTRPM4_{NBA}$ with NBA shown in purple stick representation in the binding site. (e) Zoom-in of NBA with the cryo-EM density in mesh representation. (f) NBA in sphere representation is shown in the HsTRPM4 binding pocket shown in surface representation. (g) The structure of $HsTRPM4_{IBA}$ with IBA shown in cyan stick representation in the binding site. (h) Zoom-in of NBA with the cryo-EM density in mesh representation. (i) IBA in sphere representation is shown in the HsTRPM4 binding pocket in surface representation. (j) Superimposition of $HsTRPM4_{apo}$ in light gray, $HsTRPM4_{NBA}$ in purple and $HsTRPM4_{IBA}$ in cyan. Two views of the structures are shown. (k) Pore radius for $HsTRPM4_{apo}$, $HsTRPM4_{NBA}$ and $HsTRPM4_{IBA}$, all calculated using MOLE. In the top right corner is the pore-forming helices in $HsTRPM4_{apo}$. The pore profile is shown as a space-filling model (grey).

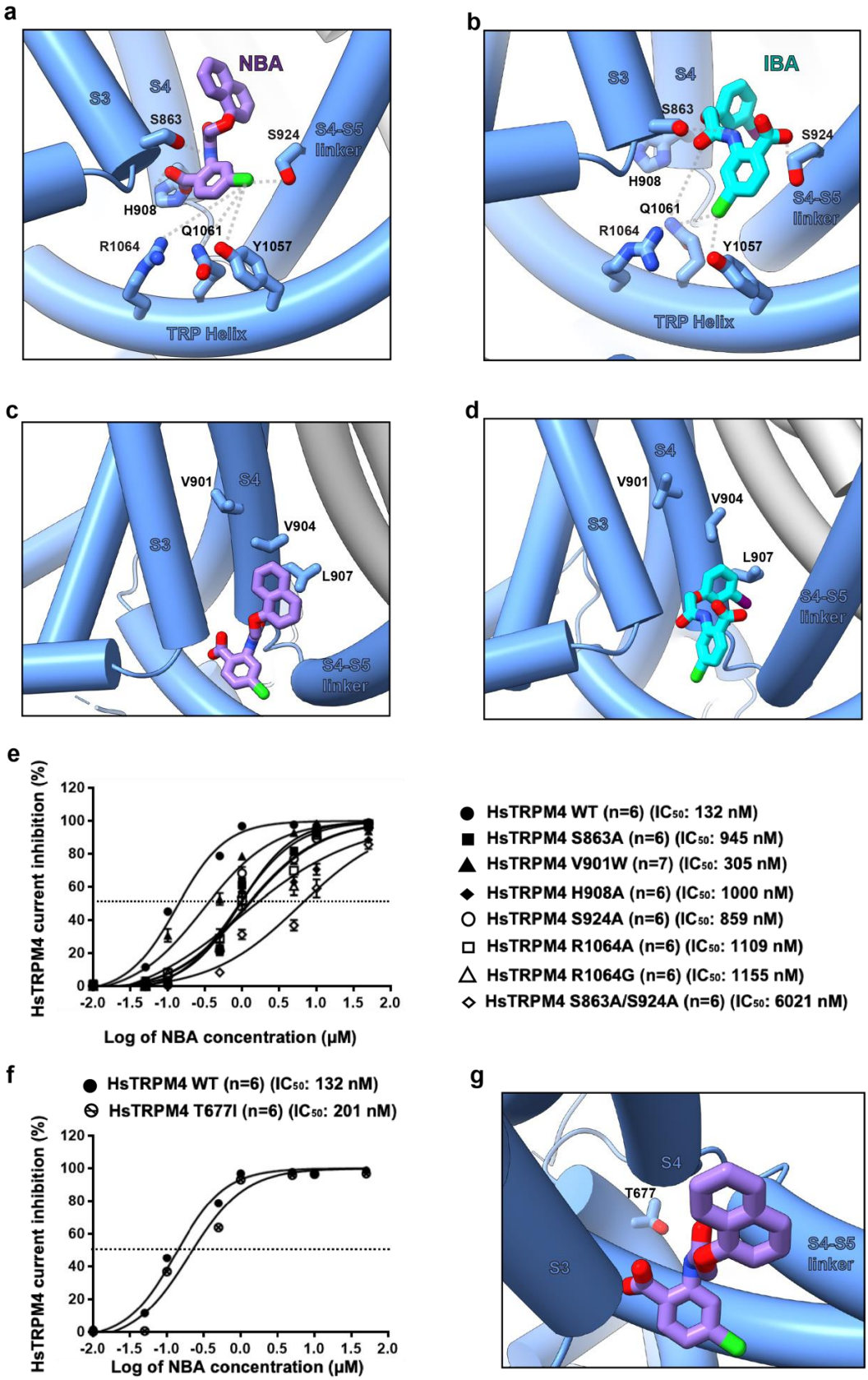


**Figure 3**: Amino acid interactions in the drug binding pocket. (a) Amino acid residues of HsTRPM4 involved in interactions with the anthranilic acid moiety of NBA (in purple) and (b)

IBA (cyan) are shown. (c) Amino acid residues of HsTRPM4 involved in hydrophobic interactions with NBA (in purple) and (d) IBA (in cyan) are shown. (e- h) Effect of HsTRPM4 variants on NBA inhibition. (e) NBA dose-response curves of wildtype (WT) and a few variants of the predicted binding pocket of HsTRPM4 channel generated in this study. (n): number of cells. (f and g) NBA dose-response curves of wildtype (WT) and a T677I variant outside the drug binding pocket of the HsTRPM4 channel. (n): number of cells.

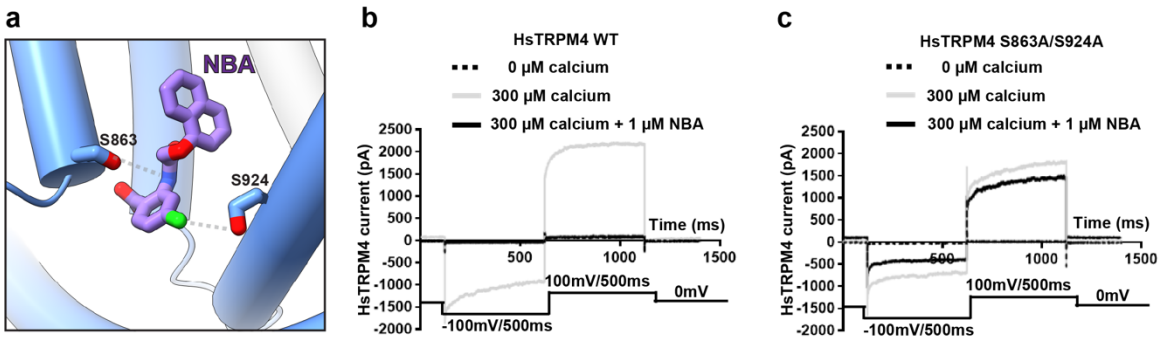


**Figure 4**: A double mutation in the drug-binding pocket alleviates inhibition. (a) Locations of S863 and S924 in the drug binding pocket (b and c) Representative traces of wildtype (WT) and variant HsTRPM4 currents: S863A/S924A in the absence of calcium (dotted black line), in the presence of calcium (grey line) and in the presence of calcium and 1 µM of NBA (black line).

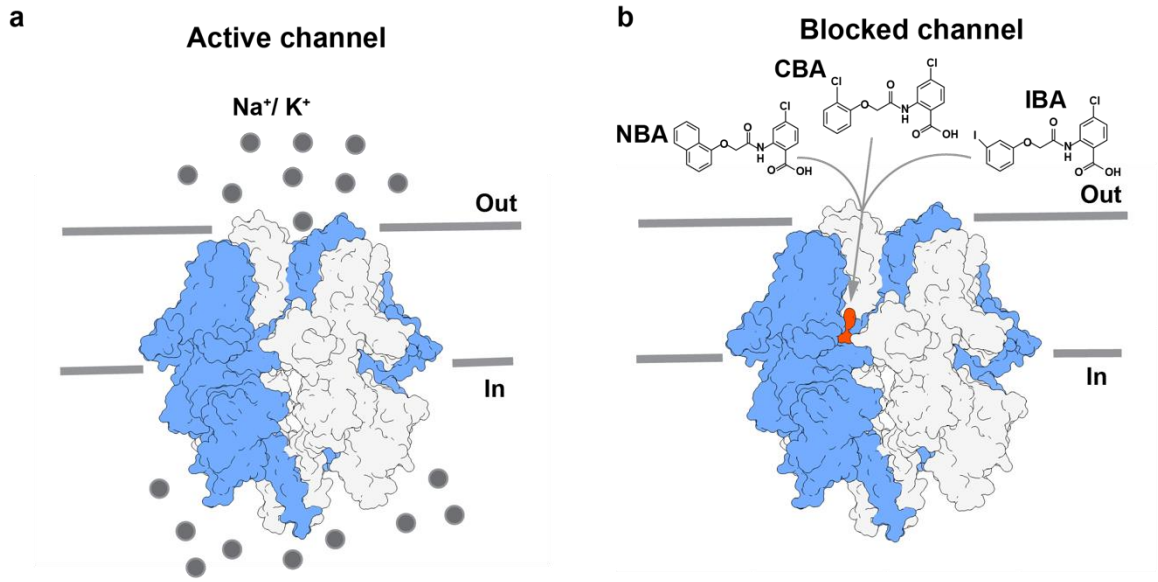


**Figure 5**: The binding of anthranilic acid drugs such as NBA, CBA and IBA in the TRPPM4 drug binding site leads to channel blocking, as shown in a and b.

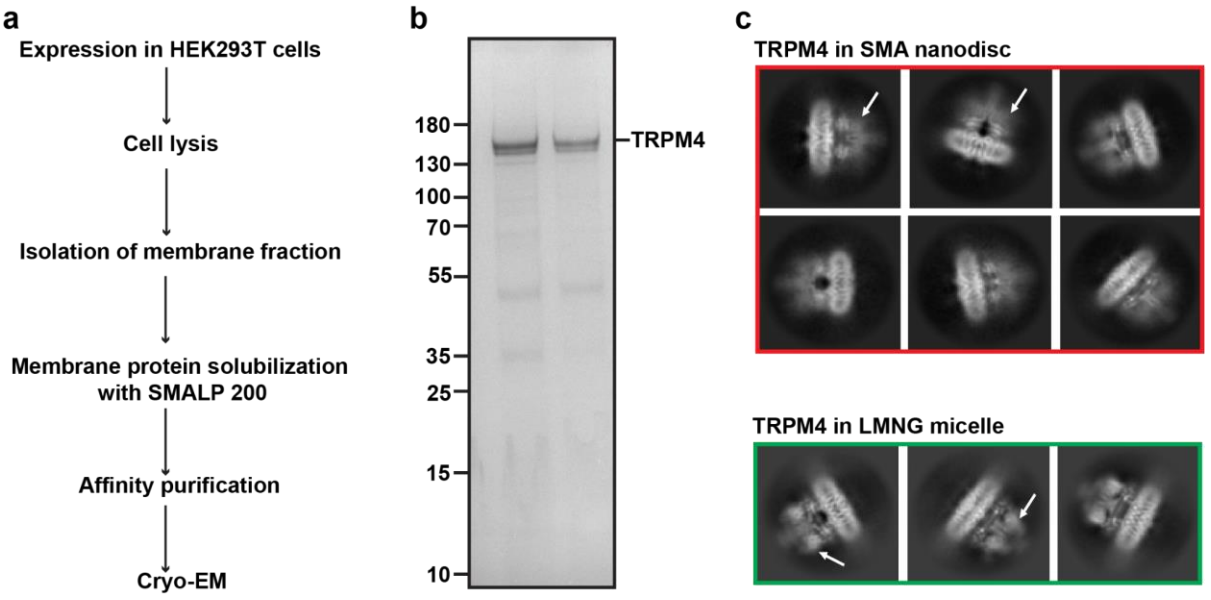


**Supplementary Fig. 1**: Purification of TRPM4 in SMA-extracted native lipid nanodiscs. (a) Biochemical workflow for the isolation of and purification of HsTRPM4 in native lipid nanodiscs using SMA (SMALP-200). B) SDS-PAGE gel of purified HsTRPM4 following affinity purification. (c) Cryo-EM 2D class averages of TRPM4 in SMA-extracted native lipid nanodiscs and in LMNG detergent micelles. White arrows indicate the positions of MHR3/4 in the TRPM4 2D classes.

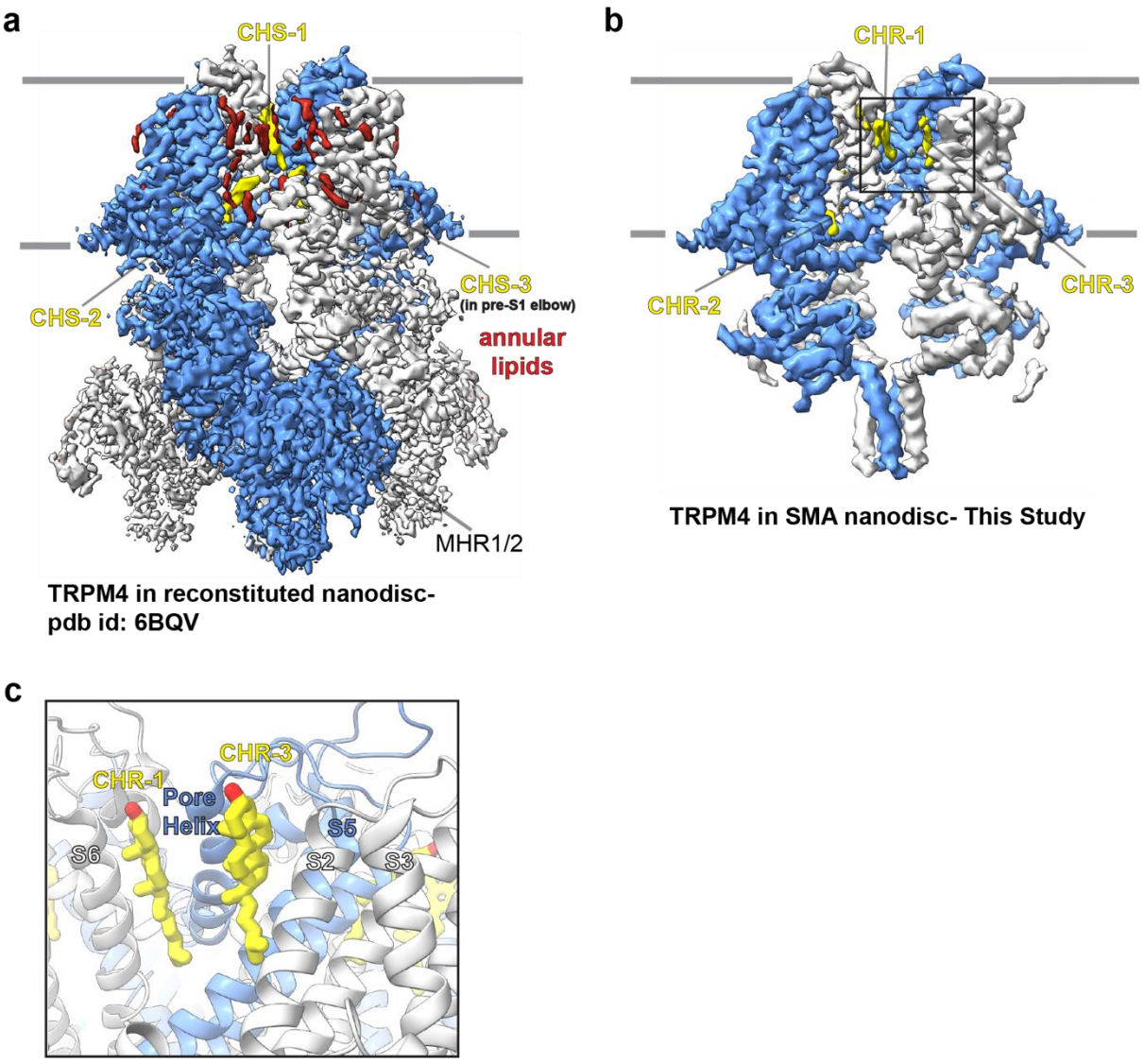


**Supplementary Fig. 2**: Comparison of the annular lipid environment between the cryo-EM maps of HsTRPM4 in reconstituted lipid nanodiscs [26] (a) and in SMA-extracted native lipid nanodiscs (b) CHS represents cholesteryl hemisuccinate in (a) and CHR represents cholesterol in (b). (c) Location of CHR-1 and CHR-3 is shown from the cryo-EM structure of HsTRPM4 in native lipid nanodiscs.

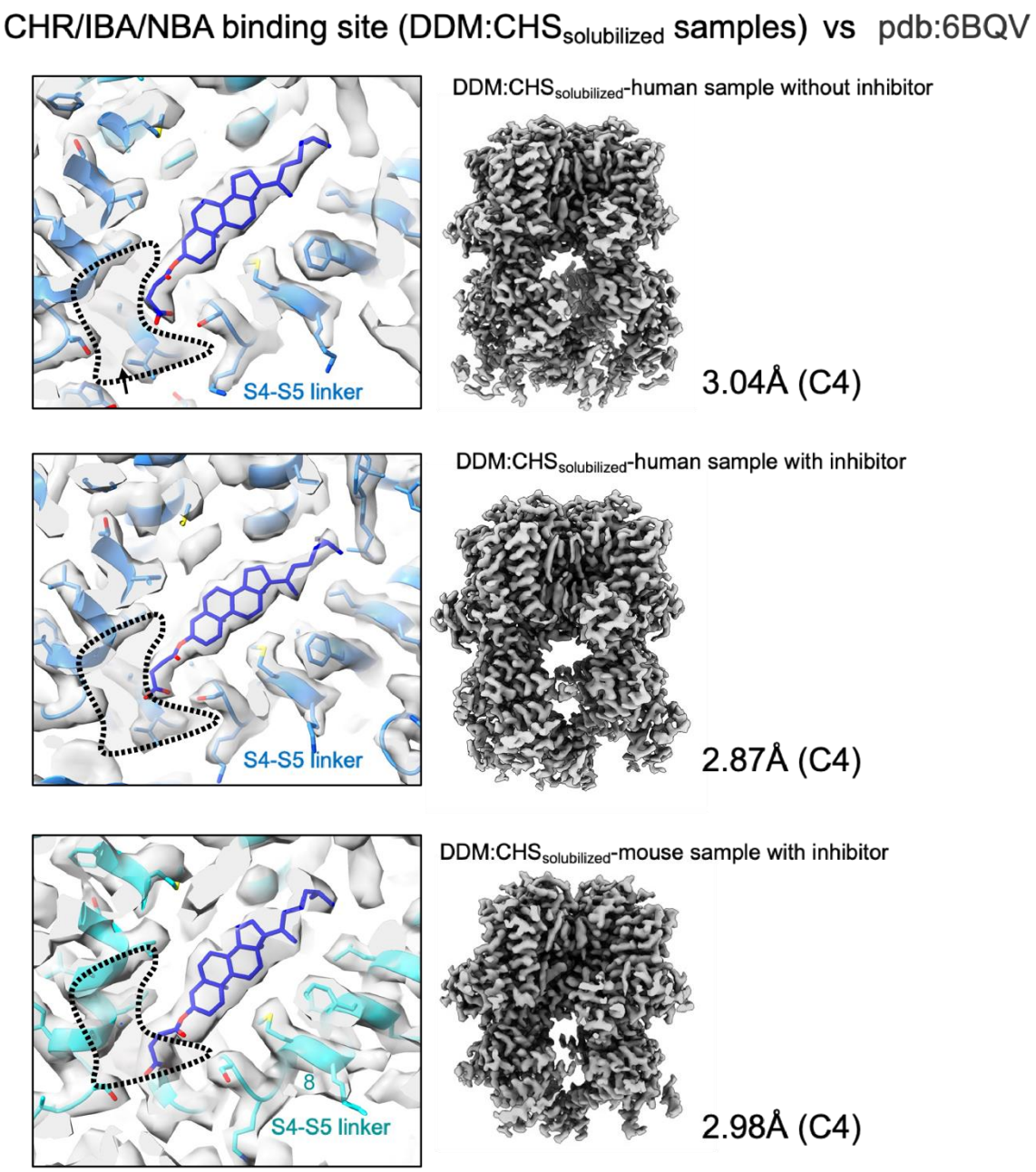


**Supplementary Fig. 3**: CryoEM maps of detergent-solubilized TRPM4 generated in this study highlighting the presence of CHS in the drug binding site when fitted with the published model (pdb-id; 6BQV)

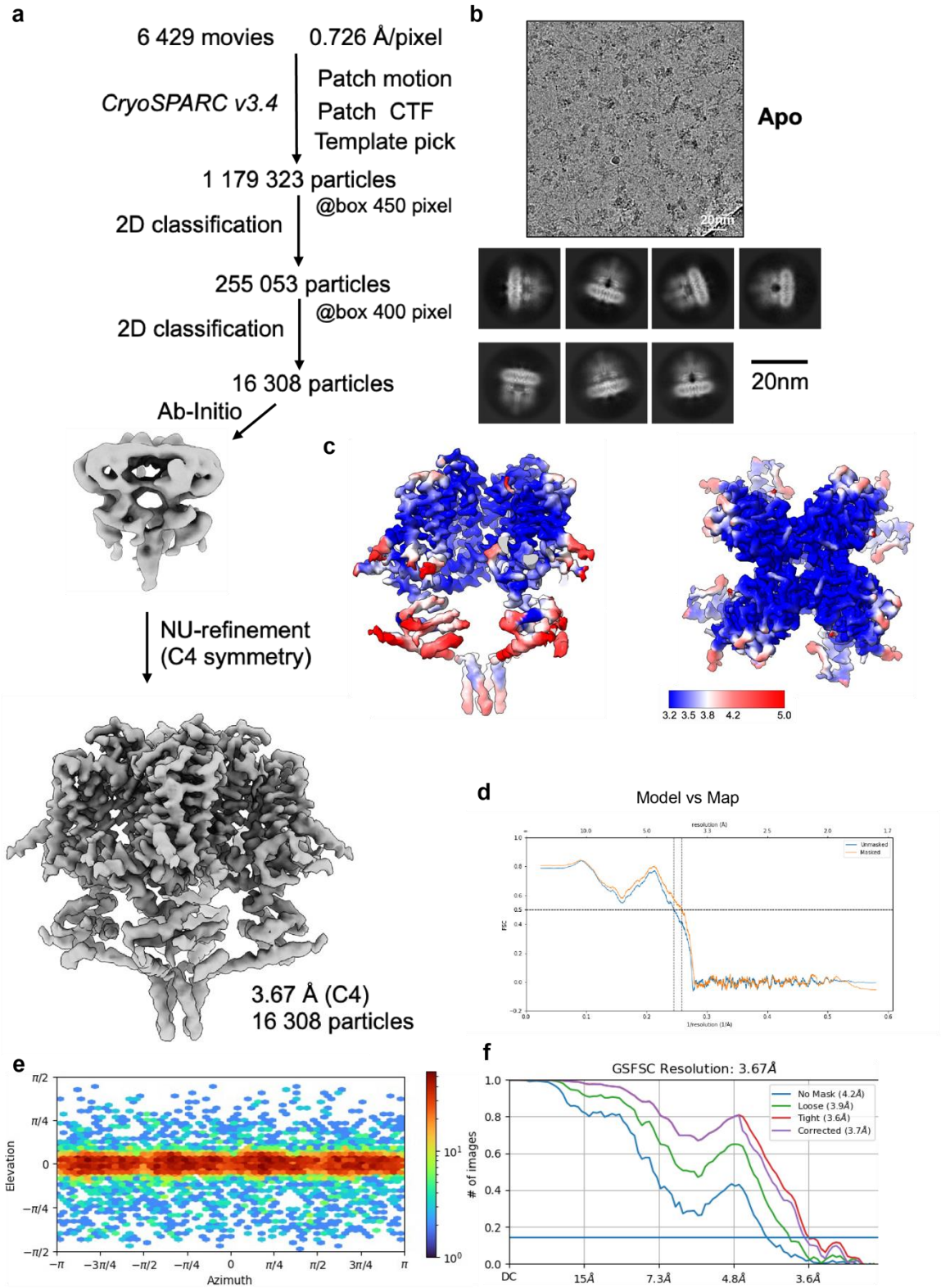


**Supplementary Fig. 4**: Cryo-EM data processing workflow and map resolution (a) The image processing workflow of HsTRPM4$_{apo}$. (b) micrograph and 2D classes (c) Local resolution (d) Model vs map FSC curves. (e) particle direction distribution. (f) FSC curves.

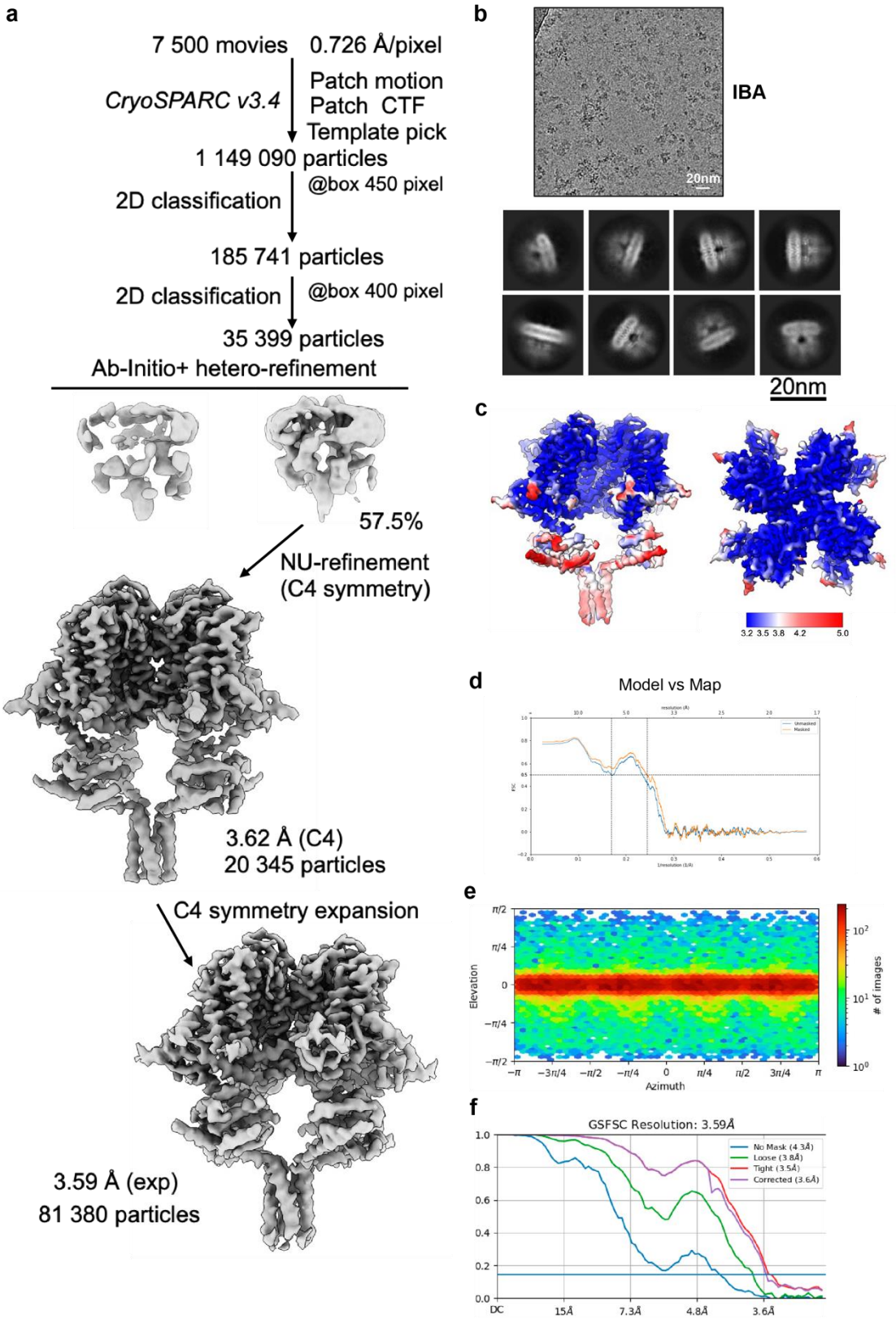


**Supplementary Fig. 5**: Cryo-EM data processing workflow and 3D reconstructions (a) The image processing workflow of HsTRPM4$_{IBA}$. (b) Micrograph and 2D classes. (c) Local resolution. (d) Model vs map FSC curves. (e) particle direction distribution. (f) FSC curves.

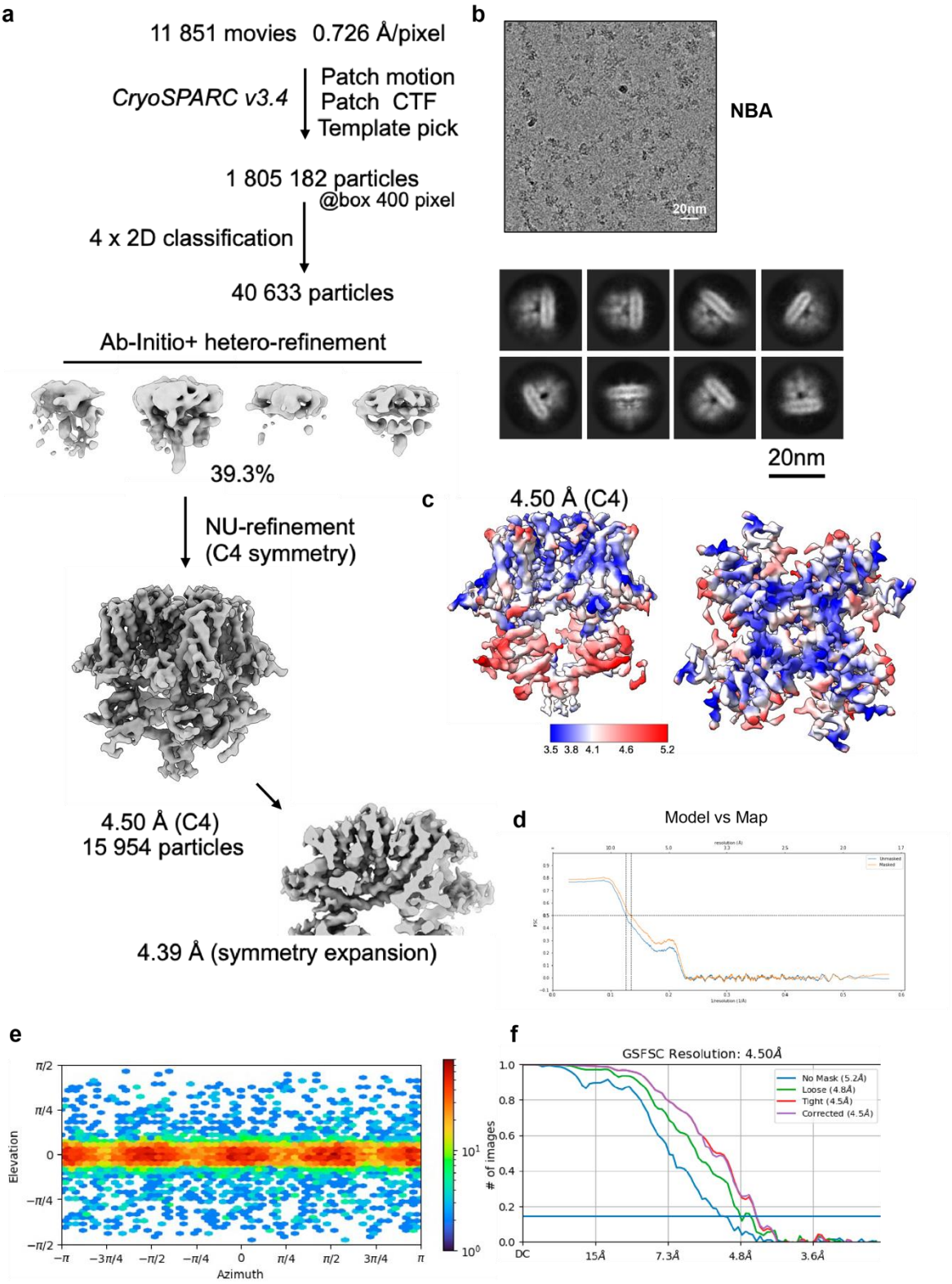


**Supplementary Fig. 6**: Cryo-EM data processing workflow and 3D reconstructions. (a) The image processing workflow of HsTRPM4$_{NBA}$. (b) Micrograph and 2D classes. (c) Local resolution. (d) Model vs map FSC curves. (e) particle direction distribution. (f) FSC curves.

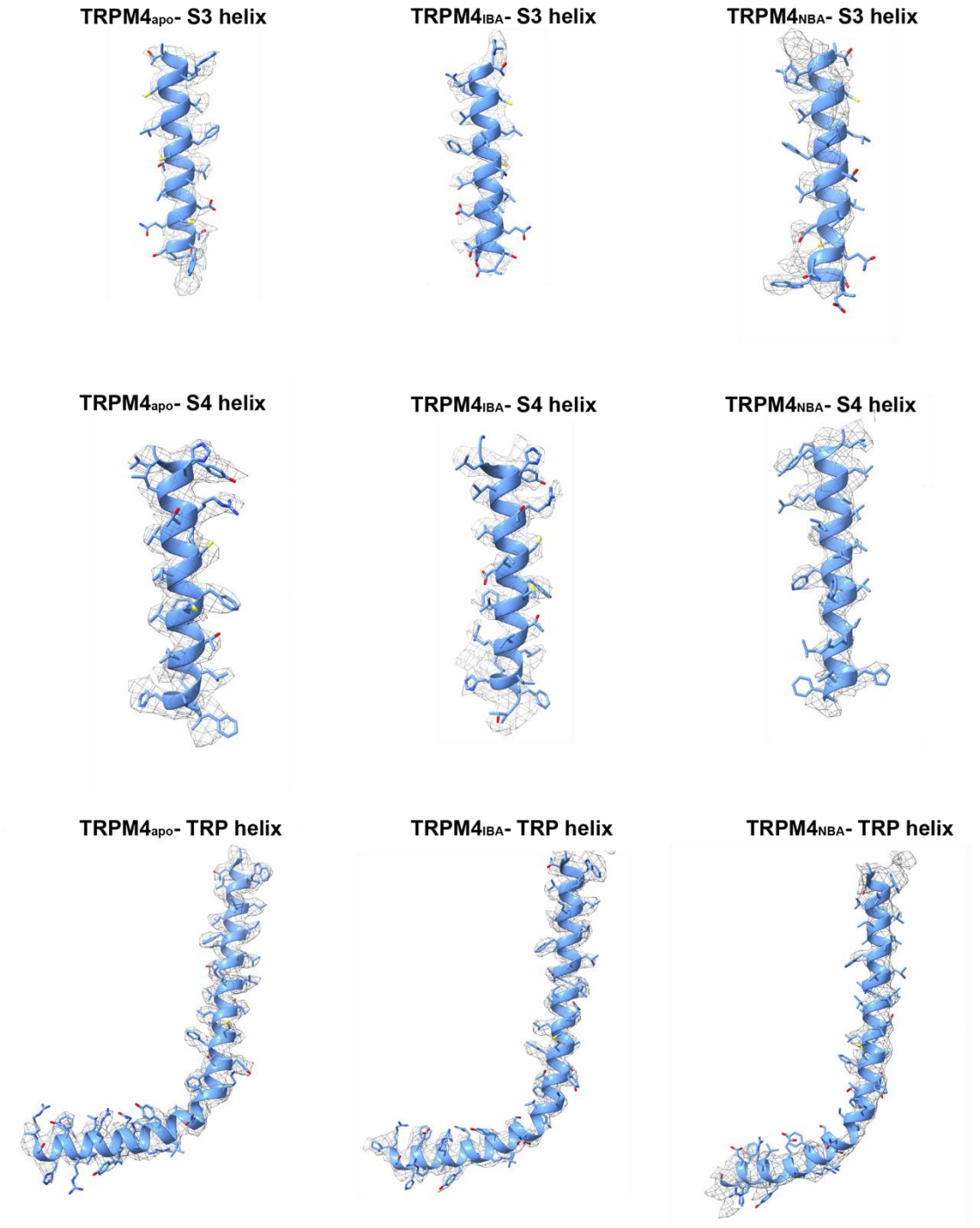


**Supplementary Fig. 7**: Zoom-in view of the cryo-EM maps of structural elements HsTRPM4$_{apo}$, HsTRPM4$_{IBA}$ and HsTRPM4$_{NBA}$.

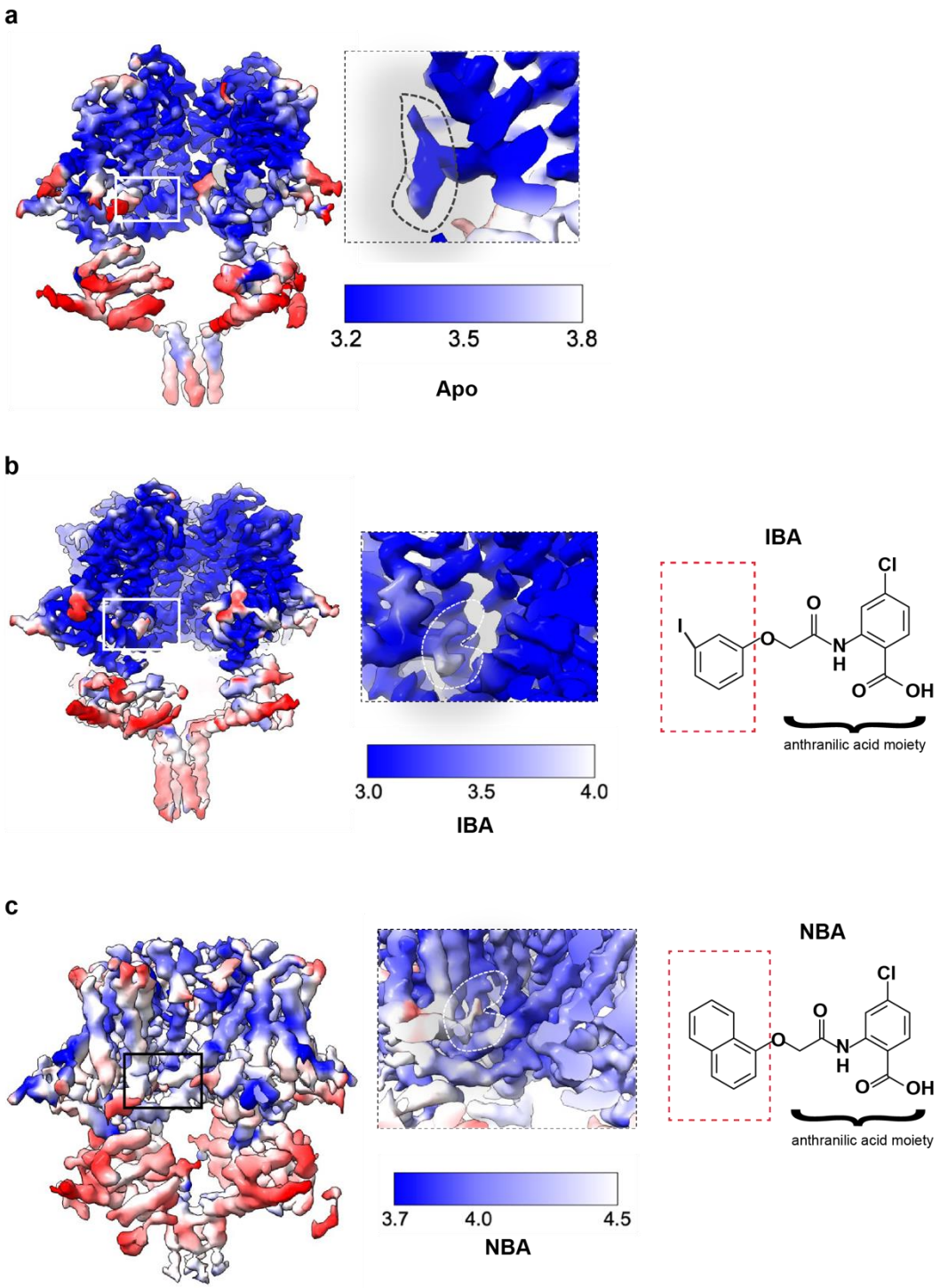


**Supplementary Fig. 8**: Local resolution maps of SMA solubilized HsTRPM4 generated in this study. (a) Map for the $HsTRPM4_{apo}$ with the density contained in the drug binding site highlighted. (b) Map for $HsTRPM4_{IBA}$ with the density contained in the drug binding site highlighted. The chemical structure of IBA is shown on the right. (c) Map for $HsTRPM4_{NBA}$ with

the density contained in the drug binding site highlighted. The chemical structure of NBA is shown on the right.

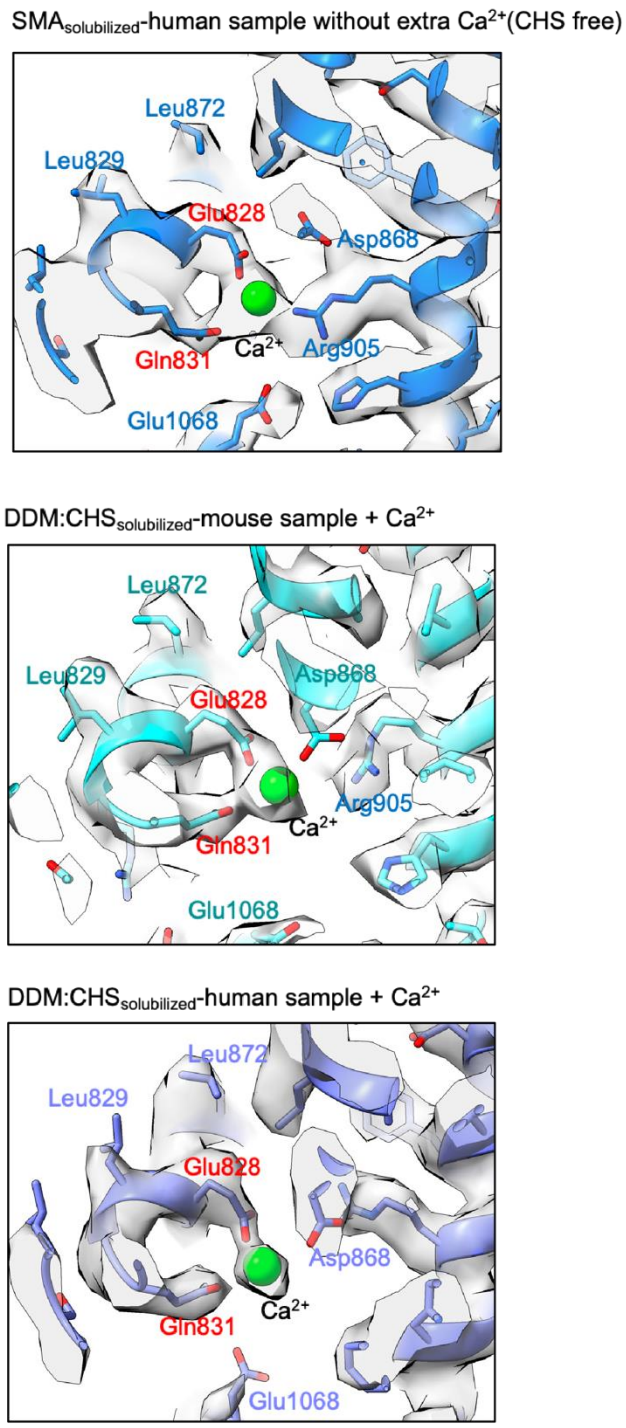


**Supplementary Fig. 9**: Identification of cryo-EM densities for $Ca^{2+}$ ions in the maps generated in this study. The published HsTRPM4 model (pdb-id: 6BQV)[26] is fitted into each map. Clear density is observed for $Ca^{2+}$ in the map for SMA solubilized human TRPM4 sample without addition of extra calcium which is comparable to the density shown for detergent solubilized mouse and human TRPM4 with calcium added to the sample.

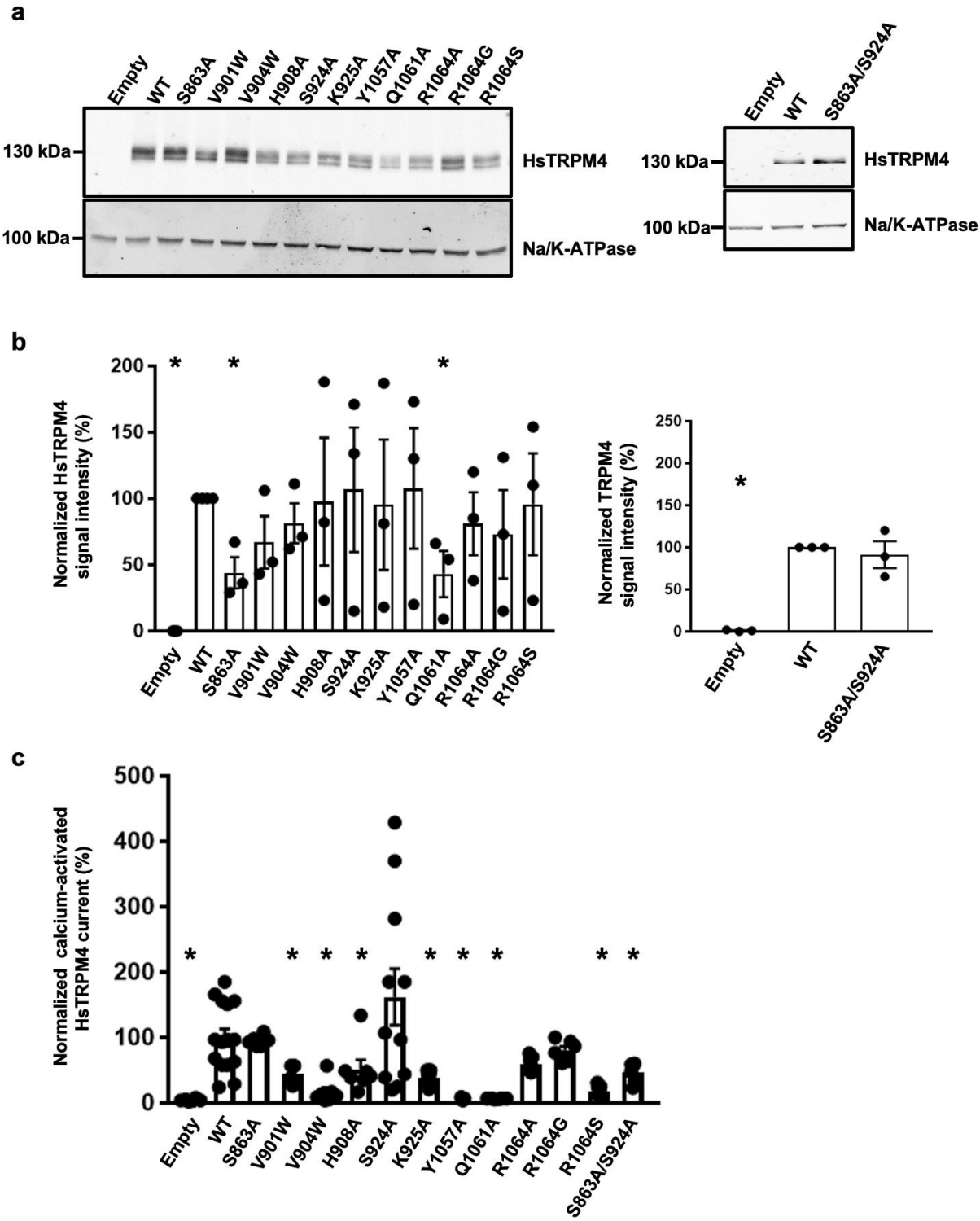


384

385 **Supplementary Fig. 10**: Expression of HsTRPM4 variants. (a) Western blot showing the

386 expression of wildtype (WT) and HsTRPM4 variants expressed in HEK293 cells. (b)

387 Graphical plot of relative western blot intensities between wildtype (WT) and HsTRPM4

388 variants. (*) represents the p-value <0.05 compared to the wildtype condition. Experiments

have been done in triplicate. (c) Graphical plot of normalized recorded calcium-activated TRPM4 currents for the wildtype (WT) and HsTRPM4 variants. (*) represents the p-value < 0.05 compared to the wildtype condition. At least 5 cells per condition have been recorded.

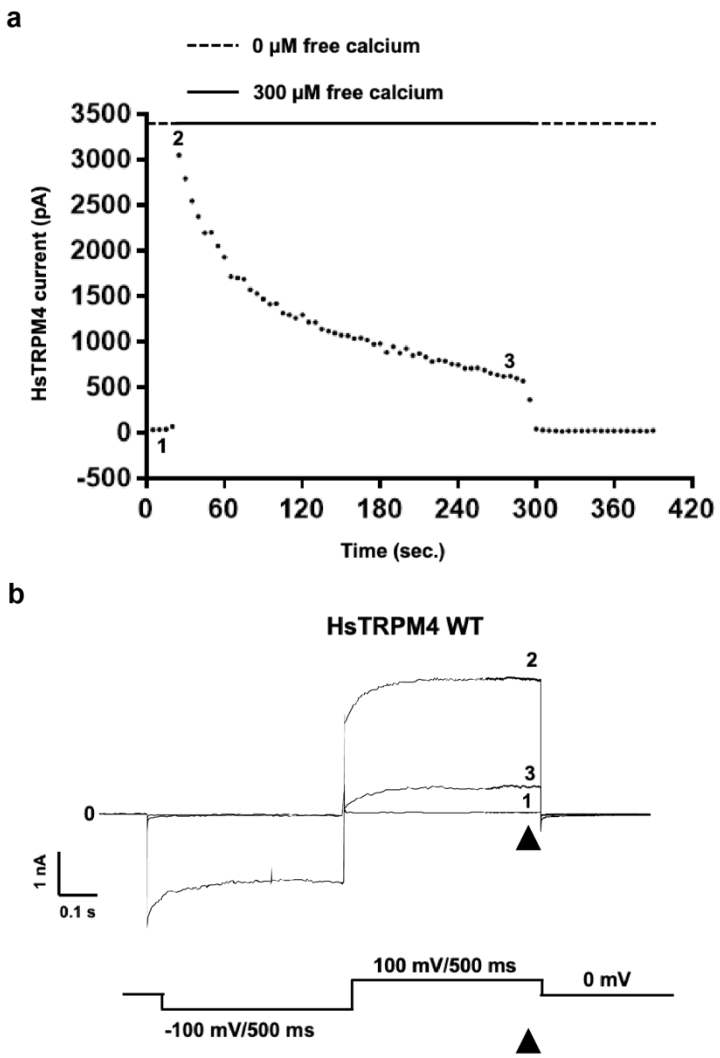


**Supplementary Fig. 11**: Time course of wildtype sodium calcium-activated HsTRPM4 current. (a) Example of a time course of sodium calcium-activated HsTRPM4 wildtype (WT) current. Each point corresponds to the amplitude of the current measured at the end of the second pulse of the protocol shown in (b) (black triangles). (b) Currents from three different time points 1, 2, and 3 from the time course shown in (a).

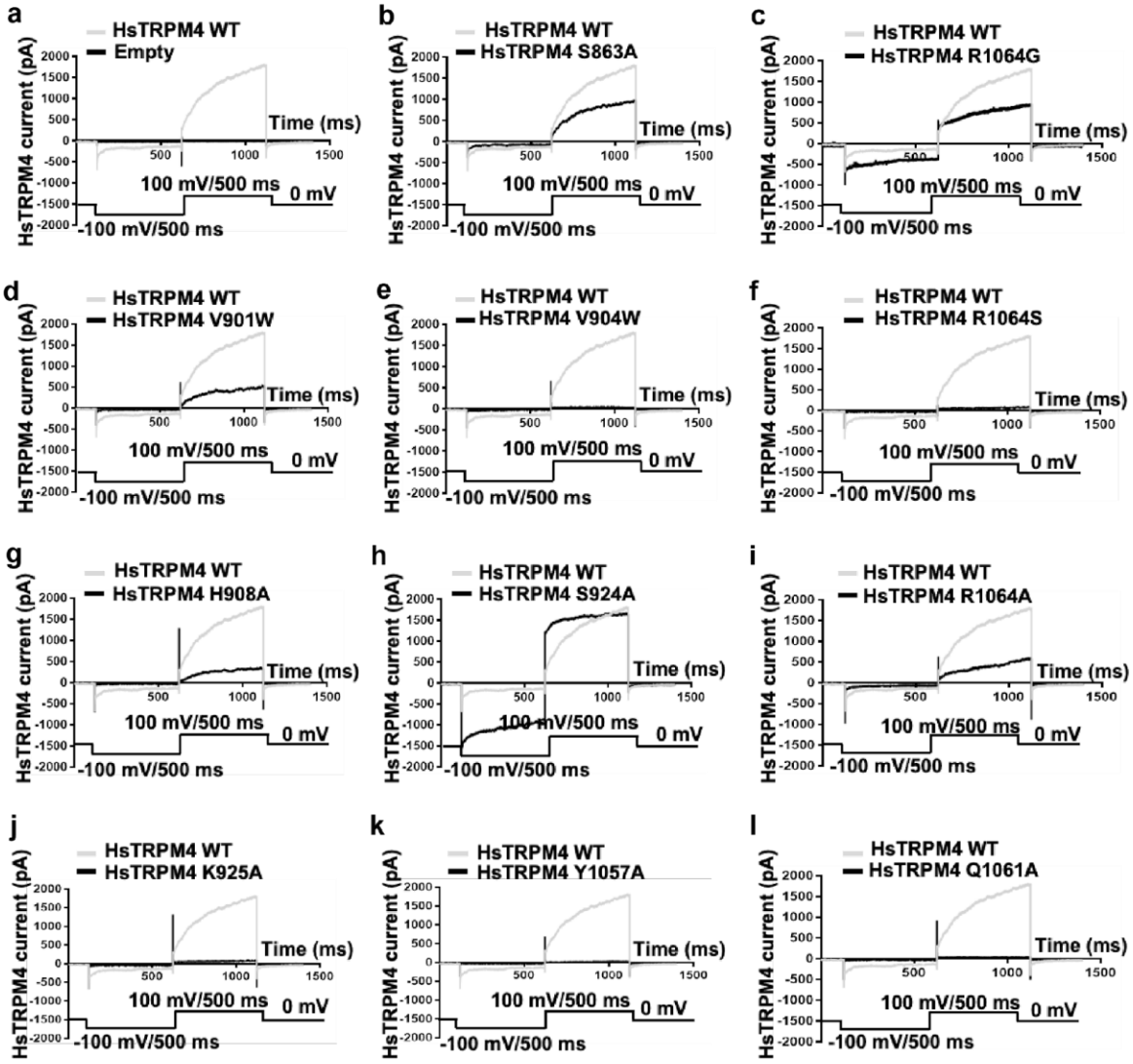


**Supplementary Fig. 12**: Sodium calcium-activated HsTRPM4 currents. (a to f) Representative traces of wildtype (WT) and variants HsTRPM4 currents: S863A, V901W, V904W, H908A, and S924A. (g to l) Representative traces of wildtype (WT) and variants HsTRPM4 currents: K925A, Y1057A, Q1061A, R1064A, R1064G, and R1064S.

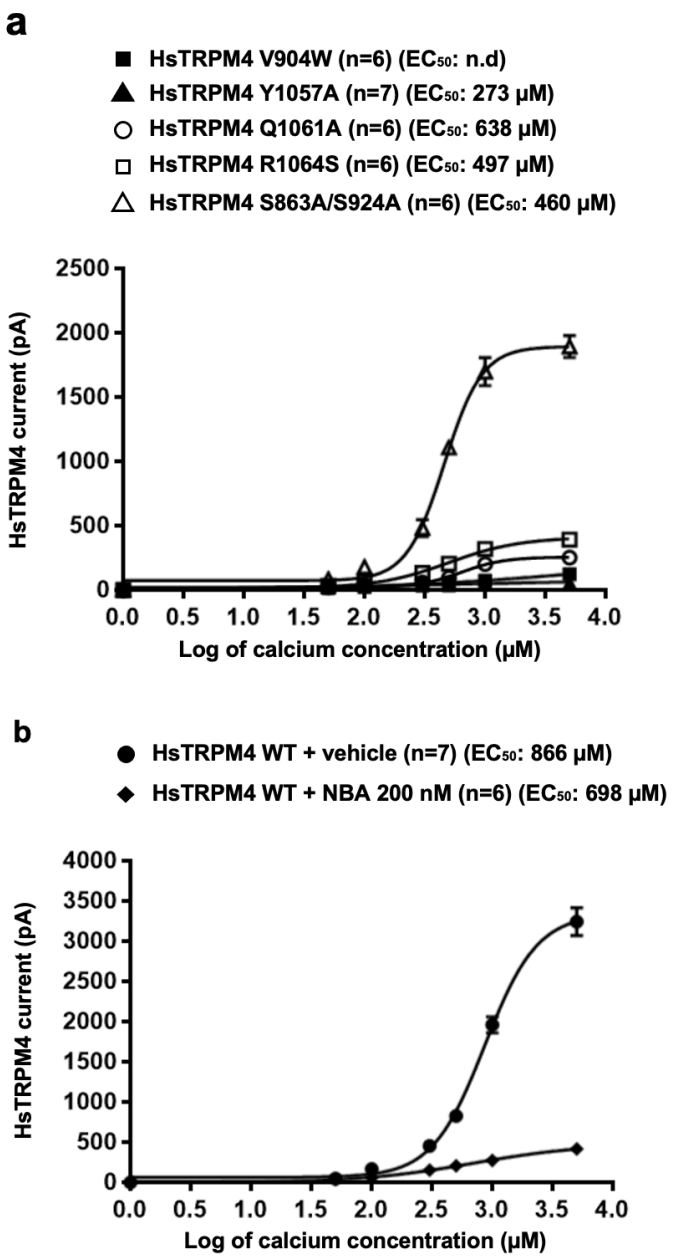


**Supplementary Fig. 13**: Calcium sensitivity curves of wildtype and variant HsTRPM4. (a) Calcium sensitivity curves of a few loss-of-function HsTRPM4 variants. (n): number of cells. n.d: not determinable. (b) Effect of NBA (200 nM) on the calcium sensitivity on wildtype (WT) HsTRPM4 channels.

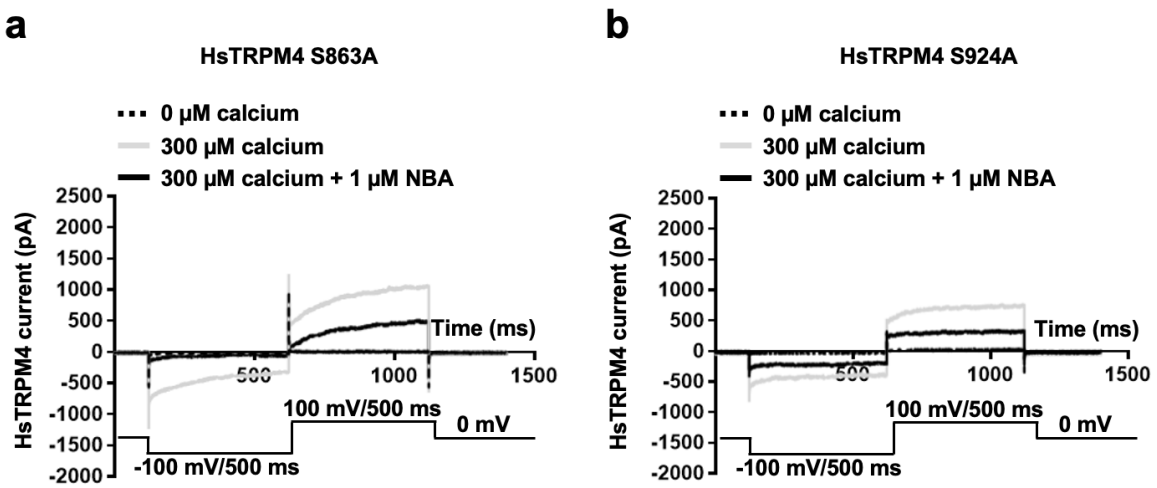


**Supplementary Fig. 14**: Sodium calcium-activated HsTRPM4 currents. (a and b) Representative traces of variants HsTRPM4 current: S863A and S924A in the absence of calcium (dotted black line), in the presence of calcium (grey line) and in the presence of calcium and 1 µM of NBA (black line).

## References


1. Clapham, D. E. TRP channels as cellular sensors. *Nature* **426**, 517–524 (2003).
2. Song, M. Y. & Yuan, J. X.-J. Introduction to TRP channels: structure, function, and regulation. *Adv. Exp. Med. Biol.* **661**, 99–108 (2010).
3. Koivisto, A.-P., Belvisi, M. G., Gaudet, R. & Szallasi, A. Advances in TRP channel drug discovery: from target validation to clinical studies. *Nat. Rev. Drug Discov.* **21**, 41–59 (2022).
4. Fallah, H. P. *et al.* A Review on the Role of TRP Channels and Their Potential as Drug Targets_An Insight Into the TRP Channel Drug Discovery Methodologies. *Front. Pharmacol.* **13**, 914499 (2022).
5. Launay, P. *et al.* TRPM4 is a Ca2+-activated nonselective cation channel mediating cell membrane depolarization. *Cell* **109**, 397–407 (2002).
6. Nilius, B. *et al.* Voltage dependence of the Ca2+-activated cation channel TRPM4. *J. Biol. Chem.* **278**, 30813–30820 (2003).
7. Wang, C., Naruse, K. & Takahashi, K. Role of the TRPM4 Channel in Cardiovascular Physiology and Pathophysiology. *Cells* **7**, (2018).
8. Guinamard, R., Demion, M. & Launay, P. Physiological roles of the TRPM4 channel extracted from background currents. *Physiology* **25**, 155–164 (2010).
9. Cheng, H. *et al.* TRPM4 controls insulin secretion in pancreatic beta-cells. *Cell Calcium* **41**, 51–61 (2007).
10. Bianchi, B., Ozhathil, L. C., Medeiros-Domingo, A., Gollob, M. H. & Abriel, H. Four TRPM4 Cation Channel Mutations Found in Cardiac Conduction Diseases Lead to Altered Protein Stability. *Front. Physiol.* **9**, 177 (2018).
11. Liu, H. *et al.* Gain-of-function mutations in TRPM4 cause autosomal dominant isolated cardiac conduction disease. *Circ. Cardiovasc. Genet.* **3**, 374–385 (2010).
12. Liu, H. *et al.* Molecular genetics and functional anomalies in a series of 248 Brugada cases with 11 mutations in the TRPM4 channel. *PLoS One* **8**, e54131 (2013).

13. Janin, A. *et al.* TRPM4 mutations to cause autosomal recessive and not autosomal dominant Brugada type 1 syndrome. *Eur. J. Med. Genet.* **62**, 103527 (2019).
14. Stallmeyer, B. *et al.* Mutational spectrum in the Ca(2+)--activated cation channel gene TRPM4 in patients with cardiac conductance disturbances. *Hum. Mutat.* **33**, 109–117 (2012).
15. Hof, T. *et al.* TRPM4 non-selective cation channel variants in long QT syndrome. *BMC Med. Genet.* **18**, 31 (2017).
16. Borgström, A., Peinelt, C. & Stokłosa, P. TRPM4 in Cancer—A New Potential Drug Target. *Biomolecules* **11**, 229 (2021).
17. Zhao, Y., McVeigh, B. M. & Moiseenkova-Bell, V. Y. Structural Pharmacology of TRP Channels. *J. Mol. Biol.* **433**, 166914 (2021).
18. Guinamard, R., Hof, T. & Del Negro, C. A. The TRPM4 channel inhibitor 9-phenanthrol. *Br. J. Pharmacol.* **171**, 1600–1613 (2014).
19. Arullampalam, P. *et al.* Species-Specific Effects of Cation Channel TRPM4 Small-Molecule Inhibitors. *Front. Pharmacol.* **12**, 712354 (2021).
20. Ozhathil, L. C. *et al.* Identification of potent and selective small molecule inhibitors of the cation channel TRPM4. *Br. J. Pharmacol.* **175**, 2504–2519 (2018).
21. Guinamard, R., Simard, C. & Del Negro, C. Flufenamic acid as an ion channel modulator. *Pharmacol. Ther.* **138**, 272–284 (2013).
22. Ruan, Z. *et al.* Structures of the TRPM5 channel elucidate mechanisms of activation and inhibition. *Nat. Struct. Mol. Biol.* **28**, 604–613 (2021).
23. Zhao, C. *et al.* Structures of a mammalian TRPM8 in closed state. *Nat. Commun.* **13**, 3113 (2022).
24. Su, N. *et al.* Structural mechanisms of TRPV2 modulation by endogenous and exogenous ligands. *Nat. Chem. Biol.* **19**, 72–80 (2023).
25. Guo, J. *et al.* Structures of the calcium-activated, non-selective cation channel TRPM4. *Nature* **552**, 205–209 (2017).
26. Autzen, H. E. *et al.* Structure of the human TRPM4 ion channel in a lipid nanodisc.

*Science* **359**, 228–232 (2018).

27. Winkler, P. A., Huang, Y., Sun, W., Du, J. & Lü, W. Electron cryo-microscopy structure of a human TRPM4 channel. *Nature* **552**, 200–204 (2017).
28. Duan, J. *et al.* Structure of full-length human TRPM4. *Proc. Natl. Acad. Sci. U. S. A.* **115**, 2377–2382 (2018).
29. Dörr, J. M. *et al.* The styrene-maleic acid copolymer: a versatile tool in membrane research. *Eur. Biophys. J.* **45**, 3–21 (2016).
30. Syam, N. *et al.* Variants of Transient Receptor Potential Melastatin Member 4 in Childhood Atrioventricular Block. *J. Am. Heart Assoc.* **5**, (2016).
31. Smith, A. A. A. *et al.* Lipid Nanodiscs via Ordered Copolymers. *Chem* **6**, 2782–2795 (2020).
32. Yin, Y. *et al.* Structural basis of cooling agent and lipid sensing by the cold-activated TRPM8 channel. *Science* **363**, (2019).
33. Wang, L. *et al.* Structures and gating mechanism of human TRPM2. *Science* **362**, (2018).

## Methods

### Synthesis of 4-Chloro-2-(2-(3-iodophenoxy)acetamido)benzoic acid (IBA)

*General Remarks*

Reagents and organic solvents were purchased from commercial suppliers and used without further purification. Deionized water produced in house or commercially available Milli-Q® water was used depending on the application. Aqueous solutions of sodium hydroxide, hydrogen chloride, saturated ammonium chloride, saturated sodium chloride (brine) were prepared with deionized water. Thin layer chromatography (TLC) was performed using Macherey-Nagel ALUGRAM® Xtra SIL G/$UV_{254}$ plates coated with 0.20 mm silica gel 60 containing fluorescent indicator. High pressure liquid chromatography (HPLC) was performed using a Thermo Fisher Scientific UltiMate 3000 RSLCnano System composed of a DIONEX UltiMate 3000 Pump, a DIONEX UltiMate 3000 Sampler, a DIONEX UltiMate 3000 Column Compartment and a DIONEX UltiMate 3000 Diode Array Detector. HPLC measurements were conducted using Milli-Q® water (+ 0.1 % TFA) and acetonitrile (+ 0.1 % TFA) as eluents and an Acclaim™ 120 C18 column (Thermo Scientific™). Flash column chromatography (LC) was performed using the Teledyne Isco Combi*Flash*©*Rf*+ system. Teledyne Isco Redi*Sep*©*Rf* dry load cartridges were used for the preparation of dry loads. If not stated otherwise, dry loads were prepared on silica gel. Teledyne Isco Silica Redi*Sep*©*Rf* prepacked silica flash columns of two sizes (24g and 80g) were used. Nuclear magnetic resonance spectroscopy (NMR) was performed at the Departement of Chemistry, Biochemistry and Pharmaceutical Sciences, Universität Bern (Furrer Group) using a Bruker AVANCE III HD 300 GA spectrometer with a magnetic field of 7.05 Tesla and operating frequencies of 300.13 MHz for $^{1}$H measurements and 75.48 MHz for $^{13}$C measurements. High resolution mass spectrometry (HRMS) was performed by the mass spectrometry service (Schürch group) at the Departement of Chemistry, Biochemistry and Pharmaceutical Sciences, Universität Bern. The measurements were performed using electrospray ionization (ESI) and a ThermoScientific LTQ Orbitrap XL mass spectrometer with high mass resolution ($m/\Delta m$ > 100’000) and accuracy ($\Delta m$ < 3ppm). The previously published synthetic

procedure (Ozhathil *et al*., 2018) to generate similar anthranilic anilide compounds was slightly adapted.

*Methyl 4-chloro-2-(2-chloroacetamido) benzoate*

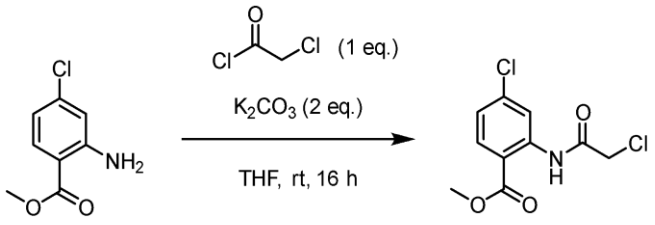


Methyl 2-amino-4-chlorobenzoate (1.7876 g, 9.6308 mmol) and potassium carbonate (2.6620 g, 19.2616 mmol, 2 eq.) were dissolved in tetrahydrofuran (150 mL) and stirred for 10 minutes at room temperature. Not all potassium carbonate dissolved completely. The mixture was then cooled in an ice bath and chloroacetyl chloride (1.0919 g, 9.6676 mmol, 0.77 mL, 1 eq.) was added dropwise via syringe. This mixture was stirred at 0 °C for 10 minutes and further stirred at room temperature for 16 hours. The reaction mixture showed a pale pink color and was monitored by thin layer chromatography (eluent: cyclohexane / ethyl acetate, 4:1). After full conversion of the starting material, water was added to the reaction mixture and the product was extracted with ethyl acetate. The combined organic phases were then washed with brine, dried over magnesium sulphate, filtered through celite and the volatiles were evaporated under reduced pressure. The crude pale-yellow and solid product was purified by flash column chromatography (eluent: cyclohexane / ethyl acetate, gradient from 0 % to 20 % ethyl acetate). The product (white powder) was dried *in vacuo*. Yield Methyl 4-chloro-2-(2-chloroacetamido) benzoate quant., 2.5 g, 9.5387 mmol. $^{1}$H NMR (300 MHz, DMSO-$d_6$) δ 11.44 (s, 1H), 8.52 (d, $J$ = 2.2 Hz, 1H), 8.00 (d, $J$ = 8.6 Hz, 1H), 7.33 (dd, $J$ = 8.6, 2.2 Hz, 1H), 4.48 (s, 2H), 3.89 (s, 3H). $^{13}$C NMR (75 MHz, DMSO-$d_6$) δ 166.75, 165.67, 140.29, 138.75, 132.51, 123.77, 119.84, 115.57, 52.82, 43.35. HRMS (ESI) *m/z* $[M+H]^+$ calculated for $C_{10}H_9Cl_2NO_3$ 262.0032, found 262.0037.

*Methyl 4-chloro-2-(2-(3-iodophenoxy)acetamido)benzoate*

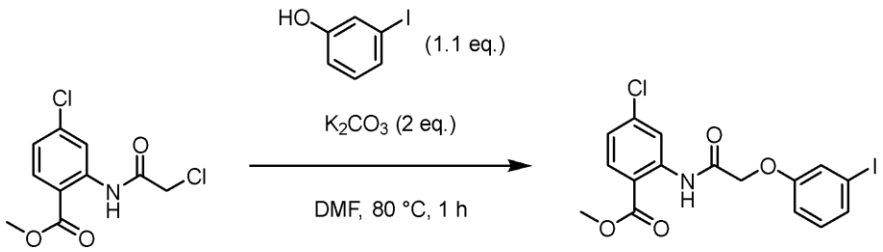


Methyl 4-chloro-2-(2-chloroacetamido) benzoate (0.3270 g, 1.2475 mmol) was dissolved in dimethylformamide (6 mL) and potassium carbonate (0.3465 g, 2.5073 mmol, 2 eq.) was added. This mixture was stirred for 10 minutes at room temperature. Not all potassium carbonate dissolved completely. 3-Iodophenol (0.3019 g, 1.3723 mmol, 1.1 eq.) was then dissolved in dimethylformamide (6 mL) and added via syringe to the reaction mixture which was stirred at 80 °C. The color of the reaction mixture changed to deep brown. The reaction was monitored by thin layer chromatography (eluent: cyclohexane / ethyl acetate, 4:1). Upon full conversion of the starting material after 60 minutes, water was added to the mixture, resulting in a brown and cloudy suspension. The product was extracted with ethyl acetate and the combined organic phases were then washed with brine, dried over magnesium sulphate, filtered through celite and the volatiles were evaporated under reduced pressure. The crude product was purified by flash column chromatography (eluent: cyclohexane / ethyl acetate, gradient from 0 % to 20 % ethyl acetate) and the purified product (white powder) was dried *in vacuo*. Yield Methyl 4-chloro-2-(2-(3-iodophenoxy)acetamido)benzoate 84 %, 0.4653 g, 1.0442 mmol. $^{1}$H NMR (300 MHz, DMSO-$d_6$) δ 11.76 (s, 1H), 8.70 (d, $J$ = 2.1 Hz, 1H), 8.01 (d, $J$ = 8.6 Hz, 1H), 7.48 (t, $J$ = 1.9 Hz, 1H), 7.40 (ddd, $J$ = 6.4, 2.5, 1.6 Hz, 1H), 7.30 (dd, $J$ = 8.6, 2.2 Hz, 1H), 7.15 – 7.09 (m, 2H), 4.79 (s, 2H), 3.91 (s, 3H). $^{13}$C NMR (75 MHz, DMSO-$d_6$) δ 167.24, 166.87, 157.61, 140.57, 138.94, 132.56, 131.50, 130.66, 123.67, 123.34, 119.33, 114.75, 114.64, 95.04, 67.35, 52.76. HRMS (ESI) *m/z* $[M+H]^+$ calculated for $C_{16}H_{13}ClINO_4$ 445.9651, found 445.9647.

*4-Chloro-2-(2-(3-iodophenoxy)acetamido)benzoic acid (IBA)*

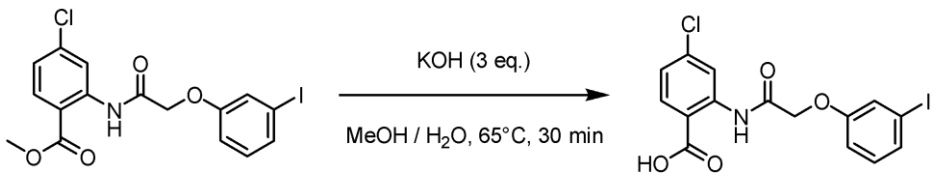


Methyl 4-chloro-2-(2-(3-iodophenoxy)acetamido)benzoate (0.4531 g, 1.0168 mmol) was dissolved in methanol (100 mL) and potassium hydroxide (0.1744 g, 3.1075 mmol, 3 eq.) was dissolved in Milli-Q® water (20 mL). The aqueous potassium hydroxide solution was added to the reaction mixture which was stirred at 65° C and progress monitored by thin layer chromatography (eluent: dichloromethane / methanol, 9:1). Upon full conversion of the starting material after 30 minutes, the reaction mixture was cooled down to room temperate. Aqueous hydrochloric acid solution (1 M, ca. 100 mL) was then added, resulting in an immediate precipitation of the product, which was filtered off using a glass filter frit (Por. 4) and the solid white product was dried *in vacuo*. Yield 4-Chloro-2-(2-(3-iodophenoxy)acetamido)benzoic acid 79 %, 0.3466 g, 0.8030 mmol. Purity (HPLC): 98.52 % (at 254 nm). $^{1}$H NMR (300 MHz, DMSO-$d_6$) δ 14.08 (s, 1H), 12.25 (s, 1H), 8.77 (d, $J$ = 2.1 Hz, 1H), 8.03 (d, $J$ = 8.6 Hz, 1H), 7.46 (m, 1H), 7.38 (dt, $J$ = 7.0, 1.7 Hz, 1H), 7.27 (dd, $J$ = 8.6, 2.2 Hz, 1H), 7.19 – 7.08 (m, 2H), 4.77 (s, 2H). $^{13}$C NMR (75 MHz, DMSO-$d_6$) δ 168.78, 167.24, 157.58, 141.12, 138.69, 133.05, 131.48, 130.55, 123.74, 123.06, 118.78, 114.94, 114.29, 95.06, 67.21. HRMS (ESI) *m/z* $[M-H]^-$ calculated for $C_{15}H_{11}ClINO_4$ 429.9349, found 429.9348.

**Description of drugs**

Stock solutions of 4-chloro-2-(2-(naphthalene-1-yloxy)acetamido)benzoic acid (NBA) and the iodo-modified congener; 4-chloro-2-(2-(3-iodo-phenoxy)acetamino)benzoic acid (IBA) were dissolved in 100% DMSO to a final concentration of 10 mM. IBA was synthesised to increase the electron densities when using the Cryo-EM approaches. Although, as proof of concept, only NBA has been used in the functional experiments presented in this study, the inhibitory efficacity of IBA has been evaluated and is the same as of NBA. NBA and IBA solutions were freshly made before each experiment. The lipophilicity of these drugs (cLog

*P*) has been calculated using the algorithms on Swiss ADME from the Swiss Institute of Bioinformatics (http://www.swissadme.ch/). The Log *P* corresponds to the ratio of the concentration of the compound at equilibrium between organic (octanol) and aqueous phases. A negative Log *P* means the compound is hydrophilic, and a positive value for Log *P* denotes a more lipophilic compound. At pH = 7.4, the NBA and IBA compounds (both protonated (carboxylic acid) and deprotonated (carboxylate) forms) tend to be lipophilic. NBA is slightly more lipophilic than IBA (consensus cLog *P* protonated/deprotonated: NBA: 3.59/3.32; IBA: 3.25/3.05).

**Plasmid constructs design and cloning**

For this study, the wild-type codon-optimized *H. sapiens* and *M. musculus* TRPM4 genes coding full-length TRPM4 were synthesized, fused to consecutive C-terminal HA (hemagglutinin)- and FLAG-tags and cloned into pCDNA-3.1 plasmid for expression in HEK293 cells by the CMV (cytomegalovirus) promoter (GenScript Biotech). Mutant variants were generated by site directed mutagenesis (GenScript Biotech).

**Protein expression and purification**

The full-length *H. sapiens* TRPM4 and *M. musculus* TRPM4 were expressed and purified from HEK293F cells grown in suspension. For expression, HEK293F cells were transfected with 1 mg of plasmid containing the TRPM4 gene per liter of cells using PEI (Polyethylenimine). The cultures were grown at 37°C and 5% $CO_2$ for 48 hours. The cultures were harvested by centrifugation at 3,000 xg for 30 mins at 4°C washed in 1x PBS followed by another round of centrifugation. The pellets were carefully resuspended in lysis buffer containing HEPES-NaOH, pH 7.5, 200 mM NaCl and supplemented with cOmplete™ EDTA-free Protease Inhibitor Cocktail (Roche). 4 tablets of protease inhibitor cocktail were added per 100ml of buffer. Following resuspension, the cells were lysed by sonication for a total of 1 min in 10 sec On and OFF cycles and an amplitude of 35%. After sonication the

membrane fraction was harvested by centrifugation using a Optima XPN-100 ultracentrifuge (Beckman Coulter) with the Ti45 rotor and spun at 70,560 × *g* for 30mins at 4°C. The resulting pellets were stored at -80°C. For solubilization of the membrane fraction with SMALP200, 12 g of pellet was resuspended in 30 ml of solubilization buffer containing HEPES-NaOH, pH 7.5, 200 mM NaCl and 0.5% SMALP200 (CubeBiotech GmbH) supplemented with 2 tablets of cOmplete™ EDTA-free Protease Inhibitor Cocktail (Roche). The resuspended pellet was homogenized manually in a 40 ml Kimble glass homogenizer (Sigma). The tube containing the mixture was then placed in a bottle with a stir bar and left to incubate at 4°C for 1 hour 30 mins. The homogenate was clarified by centrifugation for 30 min at 70,560 × *g* at 4°C in an Optima XPN Ultracentrifuge (Beckman Coulter) using a Ti-45 rotor. The supernatant, which contained soluble FLAG-tagged HsTRPM4 mixed with 1ml of Anti-FLAG® M2 affinity gel (Millipore, Billerica, MA) pre-equilibrated with wash buffer containing 25 mM HEPES-NaOH, pH 7.5, 200 mM NaCl. The beads were washed with 100 mL of wash buffer containing 25 mM HEPES-NaOH, pH 7.5, 200 mM NaCl and eluted with 4 mL elution buffer containing 25 mM HEPES-NaOH, pH 7.5, 200 mM NaCl, 120 µg/ml of 3xFLAG peptide, followed by concentration on a 100 K Amicon Ultra-15 concentrators (Millipore, Billerica, MA) to an absorbance at 280 nm of 1.0 to prepare cryo-EM grids.

For detergent solubilization, 12 g of pellet was resuspended in 30 ml of solubilization buffer containing HEPES-NaOH, pH 7.5, 200 mM NaCl, 1% n-Dodecyl-beta-Maltoside (DDM) and 0.1% Cholesteryl Hemissucinate (CHS) (Avanti Pola lipids) supplemented with 2 tablets of cOmplete™ EDTA-free Protease Inhibitor Cocktail (Roche). The resuspended pellet was homogenized manually in a 40 ml Kimble glass homogenizer (Sigma). The tube containing the mixture was then placed in a bottle with a stir bar and left to incubate at 4°C for 2 hours. The homogenate was clarified by centrifugation for 30 min at 70,560 × *g* at 4°C in an Optima XPN Ultracentrifuge (Beckman Coulter) using a Ti-45 rotor. The supernatant, which

containing soluble FLAG-tagged HsTRPM4 mixed with 1ml of Anti-FLAG® M2 affinity gel (Millipore, Billerica, MA) pre-equilibrated with wash buffer containing 25 mM HEPES-NaOH, pH 7.5, 200 mM NaCl and 1% DDM/ 0.1% CHS. The beads were washed with 100 mL of wash buffer containing 25 mM HEPES-NaOH, pH 7.5, 200 mM NaCl and 1% DDM/ 0.1% CHS and eluted with 4 mL elution buffer containing 25 mM HEPES-NaOH, pH 7.5, 200 mM NaCl, 120 µg/ml of 3xFLAG peptide and 1% DDM/ 0.1% CHS. The purified protein was run on a Superose 6 gel filtration column pre-equilibrated with 0.005% Lauryl Maltose Neopentyl Glycol (LMNG)/ 0.0005% CHS and the peak fraction was concentrated on a 100 K Amicon Ultra-15 concentrators (Millipore, Billerica, MA) to an absorbance at 280 nm of 1.0 to prepare cryo-EM grids.

**SDS-PAGE Analysis**

An SDS-PAGE analysis was performed to assess the purity of purified proteins. 15 µL of protein sample was supplemented with 5 µL of 4X NuPAGE LDS Sample Buffer (Thermo Scientific). Samples were incubated at 95°C for 10 minutes before loading on a 4-12% SurePAGE™ Bis-Tris precast gels (Witec AG). Spectra™ Prestained Protein Ladder (Thermo Scientific) (10 to 180 kDa) was also loaded on the gel to run as a size marker. Gels were run in 1X Tris-MOPS SDS running buffer (Witec AG) at 200 V for 30 minutes, washed briefly in MilliQ water and stained for 2 hours with QuickBlue Protein Stain (LuBioScience GmbH) with shaking. Gels were washed in MilliQ water before imaging on an iBright FL1500 Imaging System (Thermo Scientific).

**Cryo-EM sample preparation and data collection**

Purified TRPM4 was incubated with a final concentration of 0.2mM IBA for $TRPM4_{IBA}$ and NBA for $TRPM4_{NBA}$ for 30mins at room temperature before freezing cryo-EM grids. Cryo-EM grids were prepared by applying 3 µl of concentrated sample onto 400-mesh R1.2/1.3 UltrAuFoil grids (Quantifoil Micro Tools GmbH), which had rendered hydrophilic by glow

discharging at 15mA for 60seconds with a PELCO EasyGlow device (TED PELLA, INC). The sample were immediately blotted and plunge frozen into liquid ethane using a Vitrobot Mark IV plunge freezer (Thermo Fisher Scientific). Cryo-EM data were collected using the automated data acquisition software EPU (Thermo Fisher Scientific) on a Titan Krios G4 transmission electron microscope (Thermo Fisher Scientific), operating at 300kV and equipped with a cold-FEG electron source, a SelectrisX energy filter and a Falcon4 direct detection camera. Images were recorded in counting mode at a nominal magnification of 165kx, corresponding to a physical pixel size of 0.726 Å at the sample level. Datasets were collected at a defocus range of 0.8 to 2.5 µm with a total electron dose of 60 $e^-/Å^2$. Image data were saved as Electron Event Recordings (EER).

**Cryo-EM image processing, model building, and refinement**

The cryo-EM image processing was performed using cryoSPARC v3.4 [34].
The patch-based motion correction (cryoSPARC implementation) was used for aligning the EM movie stacks and applying dose-dependent resolution weighting to recorded movies. CTF estimation was performed using the patch-based option as well. For the data of the HsTRPM4$_{apo}$, a total of 6,429 movies at 0.726 Å per pixel were collected, and 1000 particles were manually picked and used for one round of 2D classification for template creation. Template-based automated particle picking was then used on the recorded image data, which resulted in a set of 1’719’323 particles at a size of 450 pixels. Two rounds of 2D classification were performed for the initial step of particle cleaning resulting in 255’053 particles in the first round and 16’308 in the second round. Ab-initio and non-uniform refinement yielded one 3D reconstruction with a map at 3.67 Å overall resolution in C4 symmetry (**Supplementary Fig. 4**).

For the data of the HsTRPM4$_{IBA}$, a total of 7,500 movies at 0.726 Å per pixel were collected. 2D classes from the HsTRPM$_{apo}$ dataset were used for template-based picking. Template-based automated particle picking resulted in a set of 1’149’090 particles at a size of 450

pixels. Two rounds of 2D classification were performed for the initial step of particle cleaning resulting in 185'741 particles at 400 pixels in the first round and 35'399 particles in the second round. Ab-initio and hetero-refinement refinement yielded two 3D reconstructions. One reconstruction representing 57.5% of particles was selected for further non-uniform refinement resulting in a map at 3.62 Å overall resolution in C4 symmetry. Following symmetry expansion, the overall resolution of the map could be improved to an overall resolution of 3.62 Å (**Supplementary Fig. 5**).

For the data of the $HsTRPM4_{NBA}$, a total of 11,851 movies at 0.726 Å per pixel were collected. 2D classes from the $HsTRPM_{apo}$ dataset were used for template-based picking. Template-based automated particle picking resulted in a set of 1'805'182 particles at 400 pixels. Four rounds of 2D classification were performed for the initial step of particle cleaning resulting in 40'633 particles. Ab-initio and hetero-refinement refinement yielded four 3D reconstructions. One reconstruction representing 15'954 particles was selected for further non-uniform refinement resulting in a map at 4.50 Å overall resolution in C4 symmetry from 15,954 particles (**Supplementary Fig. 6**).

Cryo-EM data was also collected for DDM/CHS solubilized mouse and human TRPM4. MmTRPM4 data was collected with 5mM Calcium chloride present in the sample. Two datasets were collected for DDM/CHS solubilized HsTRPM4 with 5mM Calcium chloride present in one sample and both 5mM Calcium chloride and 0.2mM NBA present in the other. Details of the data collection are included (**Supplementary Table 2**).

Atomic models for $HsTRPM_{apo}$, $HsTRPM4_{IBA}$ and $HsTRPM4_{NBA}$ structures mainly were built in Coot 0.9.4 [35], using a model PDB id: 6BQV as an initial model. Real-space refinement for all built models was performed using Phenix, version 1.19.2-4158 by applying a general restraints setup [36].

**Cell Culture**

TsA-201 cells were cultured with Dulbecco's Modified Eagle's culture Medium DMEM (Gibco, Basel, Switzerland) supplemented with 10% FBS, 0.5% penicillin, and streptomycin (10,000 U/mL) at 37°C in a 5% $CO_2$ incubator.

**Transfections**

Sixty mm dishes (BD Falcon, Durham, North Carolina, USA) at 80% of confluence were transiently transfected using Xtreme Gene 9™ transfection reagent (Sigma Aldrich Merck, Switzerland) and following the instructions of the manufacturer. In brief, 1,000 ng of either empty vector or HsTRPM4 WT or variants of HsTRPM4 (TRPM4 S863A, TRPM4 V901W, TRPM4 V904W, TRPM4 H908A, TRPM4 S924A, TRPM4 K925A, TRPM4 Y1057A, TRPM4 Q1061A, TRPM4 R1064A, TRPM4 R1064G, TRPM4 R1064S or TRPM4 S863A/S924A) was mixed with a solution containing 100 ng of a reporter gene coding for GFP and 1,000 ng of empty vector. The expression of GFP was used to evaluate the transfection efficiency procedure, and the empty vector was added to reach a certain amount of total cDNA to ensure an efficient transfection. These final cDNA solutions (2,100 ng) were mixed with 210 µL of opti-MEM (Gibco, Basel, Switzerland) and 6.3 µL of Xtreme Gen9™ reagent (ration 1/3). After 30 minutes at room temperature, the cDNA solutions were applied to the cells. Forty-eight hours post-transfection, the cells were harvested for the western blot experiments.

**Western-blots**

The expression of the human TRPM4 channel was assessed in whole-cell lysates. First, cells were washed with PBS 1X and then lysed for 1 hour at 4 °C in lysis buffer (50 mM HEPES pH 7.4, 1.5 mM $MgCl_2$, 150 mM NaCl, 1 mM EGTA pH 8, 10% glycerol, 1% Triton X-100, and Complete® protease inhibitor cocktail (Roche Diagnostics, Mannheim, Germany)). The pellet was discarded after centrifugation at 4 °C, 16,000 g for 15 minutes. Protein concentrations of each lysate sample were measured in triplicate by Bradford assay and

interpolated by a bovine serum albumin (BSA) standard curve. Samples were denatured at 30 °C for 37 minutes before loading on a gel. Twenty µg of protein for each sample was run at 150 V for 1 hour on 9% polyacrylamide gels. The Turbo Blot dry blot system (Biorad, Hercules, CA, USA) was used to transfer the samples to a nitrocellulose membrane. All membranes were stained with Ponceau as a qualitative check for equivalent total protein loading. Membranes were then rinsed twice with TBS 1X and blocked with 5% BSA in TBS 1X for 1 hour. After this blocking step, the membranes were incubated for 2 hours with rabbit anti-human TRPM4 antibody (epitope: $_{1137}$CRDKRESDSERLKRTSQKV$_{1155}$, Pineda, Berlin, Germany) diluted 1:1,000 in TBS 1X + 0.1% tween and mouse anti-$Na^+/K^+$ ATPase antibody (Abcam ab 7671) diluted 1:1,000 in TBS 1X + 0.1% tween. The membranes were washed 4 times in TBS 1X + 0.1% tween before incubating with fluorescent secondary antibodies. Secondary antibodies IR Dye 800 CW, anti-rabbit diluted (1:20,000) in TBS 1X + 0.1% tween and IR Dye 700 CW, anti-mouse diluted (1:20,000) in TBS 1X + 0.1% tween (LI-COR Biosciences, Lincoln, NE, USA) were added for 1 hour. After 4 washes with TBS 1X + 0.1% tween and 3 washes in TBS 1X, membranes were scanned with the FUSION FX Spectra® Infrared Imaging System (VILBER smart imaging, Marne-la-Vallée, France) to detect fluorescent protein. Subsequent quantitative analysis of protein content was achieved by measuring and comparing band densities (equivalent to fluorescence intensities of the bands) using the *Evolution-Capt software* (VILBER smart imaging, Marne-la-Vallée, France). The background was first subtracted for each band (human TRPM4 and $Na^+/K^+$ ATPase), then TRPM4 intensity was divided by the intensity of the $Na^+/K^+$ ATPase band (for a given sample) and normalized for comparison.

## Electrophysiology

### Transfections

Thirty-five mm dishes (BD Falcon, Durham, North Carolina, USA) at 80% of confluence were transiently transfected using JetPEI™ transfection reagent (Polyplus transfection, Illkirch, France) and following the instructions of the manufacturer. In brief, 500 ng of either empty

vector or HsTRPM4 WT or variants of HsTRPM4 (TRPM4 T677I, TRPM4 S863A, TRPM4 V901W, TRPM4 V904W, TRPM4 H908A, TRPM4 S924A, TRPM4 K925A, TRPM4 Y1057A, TRPM4 Q1061A, TRPM4 R1064A, TRPM4 R1064G, TRPM4 R1064S or TRPM4 S863A/S924A) was mixed with 200 ng of a reporter gene coding for GFP. Expression of GFP was used to identify transfected cells during patch clamp experiments. Coding DNAs (cDNAs from HsTRPM4 and GFP) were mixed with 4 µl of JetPEI™ and 46 µl of 150 mM NaCl. After 15 minutes at room temperature, the cDNA solutions were applied to the cells. Twenty-four hours post-transfection, the cells were plated at low density in a new 35 mm dish coated with poly-l-lysine. The cells were patched 24 hours post-platting (48 hours post-transfection).

**Inside-out patch clamp**

Electrophysiological recordings were performed in the inside-out patch-clamp configuration with patch pipettes (1 and 2 µm tip opening) pulled from 1.5 mm borosilicate glass capillaries (Zeitz-Instruments GmbH, München, Germany) using micropipette puller P 97 (Sutter Instruments, Novato, CA, United States). The tips were polished for 2–4 MΩ pipette resistance in the bath solution. The pipette solution contained 150 mM NaCl, 10 mM HEPES, and 2 mM $CaCl_2$ (pH 7.4 with NaOH). The initial bath solution with 0 calcium contained 150 mM NaCl, 10 mM HEPES, and 2 mM HEDTA (pH 7.4 with NaOH). After reaching the inside-out configuration, different solutions were perfused at the intracellular side of the membrane patch using a modified rapid solution exchanger (Perfusion Fast-Step SF-77B; Warner Instruments Corp. CT, United States).

For calcium sensitivity experiments. The first solution, applied for 3 to 5 sweeps to reach a stable current, is the bath solution (150 mM NaCl, 10 mM HEPES, and 2 mM HEDTA; pH 7.4 with NaOH) with 0 free $Ca^{2+}$. Then, to activate TRPM4 channels, a solution (150 mM NaCl, 10 mM HEPES; pH 7.4 with NaOH) containing different amounts of free $Ca^{2+}$ (50 µM, 100 µM, 300 µM, 500 µM, 1000 µM, 5000 µM) was applied. The effect of the calcium was quantified when the calcium-activated current reached stability. Finally, the bath solution with

0 µM free $Ca^{2+}$ was used to quantify the potential leak current that can occur during such recordings.

For drug dose-response experiments. The first solution, applied for 3 to 5 sweeps to reach the stable current, is the bath solution (150 mM NaCl, 10 mM HEPES, and 2 mM HEDTA; pH 7.4 with NaOH) with 0 µM free $Ca^{2+}$. Then, after stabilization of the current, a solution (150 mM NaCl, 10 mM HEPES; pH 7.4 with NaOH) containing 300 µM free $Ca^{2+}$ without compounds was applied to activated HsTRPM4 channels and recorded the calcium-activated HsTRPM4 current until its stabilization. Then, a solution (150 mM NaCl, 10 mM HEPES; pH 7.4 with NaOH) containing 300 µM free $Ca^{2+}$ and the compound at different concentrations (10 nM, 50 nM, 100 nM, 500 nM, 1000 nM, 5000 nM, 10’000 nM, 50’000 nM) were applied. The effect of the drug was quantified when the calcium-activated current reached stability. Finally, the bath solution with 0 µM free $Ca^{2+}$ was used to quantify the potential leak current that can occur during such recordings. No investigation and comparison has been done concerning the kinetic of block and washout, and only ‘’stable’’ currents have been used to calculate the percentage of inhibition.

HsTRPM4 sodium currents calcium-activated were recorded with a Multiclamp 700B amplifier (Molecular Devices, Sunnyvale CA, United States) controlled by Clampex 10 via Digidata 1332A (Molecular Devices, Sunnyvale, CA, United States). Data were low-pass filtered at 5 kHz and sampled at 10 kHz. Experiments were performed at room temperature (20–25°C). The holding potential was 0 mV. The stimulation protocol consisted of two pulses totaling 1,000 ms for measuring steady-state currents repeated at 0.2Hz (1 sweep every 5 sec.). The first pulse was at −100 mV for 500 ms, and the second was at +100 mV for 500 ms. For analysis, the effect of the compounds on sodium current calcium-activated has been calculated by averaging the last 100 ms of the second sweep at +100 mV (from the stable phase). Electrophysiology data were exported and analyzed using Prism7.05 GraphPad™ software (GraphPad by Dotmatics, San Diego, CA, USA). Concentration-response curves were fitted using the log(inhibitor) vs. response - Variable slope (four

parameters) equation (Y=Bottom + (Top-Bottom)/(1+10^((LogIC50-X)*HillSlope))) where X corresponds to the log of concentration and Y current recorded in pA.

## Data analyses and statistics

Data are represented as means ± SEM. Statistical analyses were performed using Prism7.05 GraphPad™ software (GraphPad by Dotmatics, San Diego, CA, USA). An unpaired nonparametric t-test followed by a Mann-Whitney U post-test was used to compare two unpaired groups. $p < 0.05$ was considered significant. No muti-group comparison has been performed in this study. Western blots have been done in triplicate, and at least 6 cells have been used for the different doses in electrophysiology experiments.

### Data visualization

Gel images were processed and prepared on ImageJ (Version 1.53k). Figures were rendered using PyMOL, UCSF Chimera, UCSF ChimeraX [37], and Adobe Illustrator (https://adobe.com/products/illustrator).

### Data and Code Availability

The reconstructed maps are available from the EMDB database under access codes HsTRPM4apo (EMD-19057), HsTRPM4IBA (EMD-19061), HsTRPM4NBA (EMD-19069) (EMD-19060, local). The atomic models are available in the PDB database, access codes HsTRPM4apo (PDB 8RCR), HsTRPM4IBA (8RCU) and HsTRPM4NBA (PDB 8RD9). The raw cryo-EM movies data of this work are available under access codes EMPIAR-xxxxx, EMPIAR-xxxxx, and EMPIAR-xxxxx.

## Methods-only references

34. Punjani, A., Rubinstein, J. L., Fleet, D. J. & Brubaker, M. A. cryoSPARC: algorithms for rapid unsupervised cryo-EM structure determination. *Nat. Methods* **14**, 290–296 (2017).

35. Emsley, P., Lohkamp, B., Scott, W. G. & Cowtan, K. Features and development of Coot. *Acta Crystallogr. D Biol. Crystallogr.* **66**, 486–501 (2010).

36. Liebschner, D. *et al.* Macromolecular structure determination using X-rays, neutrons and electrons: recent developments in Phenix. *Acta Crystallogr D Struct Biol* **75**, 861–877 (2019).

37. Goddard, T. D. *et al.* UCSF ChimeraX: Meeting modern challenges in visualization and analysis. *Protein Sci.* **27**, 14–25 (2018).